

Phase diagram of the triangular-lattice Potts antiferromagnet

Jesper Lykke Jacobsen^{1,2,3}, Jesús Salas^{4,5}, and Christian R. Scullard⁶

¹LPTENS, École Normale Supérieure – PSL Research University, 24 rue Lhomond, F-75231 Paris Cedex 05, France

²Sorbonne Universités, UPMC Université Paris 6, CNRS UMR 8549, F-75005 Paris, France

³Institut de Physique Théorique, CEA Saclay, 91191 Gif Sur Yvette, France

⁴Grupo de Modelización, Simulación Numérica y Matemática Industrial, Universidad Carlos III de Madrid, Avda. de la Universidad, 30, 28911 Leganés, Spain

⁵Grupo de Teorías de Campos y Física Estadística, Instituto Gregorio Millán, Universidad Carlos III de Madrid, Unidad Asociada al Instituto de Estructura de la Materia, CSIC, Madrid, Spain

⁶Lawrence Livermore National Laboratory, Livermore, CA 94550, USA

E-mail: jesper.jacobsen@ens.fr, jsalas@math.uc3m.es, scullard1@llnl.gov

Abstract. We study the phase diagram of the triangular-lattice Q -state Potts model in the real (Q, v) -plane, where $v = e^J - 1$ is the temperature variable. Our first goal is to provide an obviously missing feature of this diagram: the position of the antiferromagnetic critical curve. This curve turns out to possess a bifurcation point with two branches emerging from it, entailing important consequences for the global phase diagram. We have obtained accurate numerical estimates for the position of this curve by combining the transfer-matrix approach for strip graphs with toroidal boundary conditions and the recent method of critical polynomials. The second goal of this work is to study the corresponding A_{p-1} RSOS model on the torus, for integer $p = 4, 5, \dots, 8$. We clarify its relation to the corresponding Potts model, in particular concerning the role of boundary conditions. For certain values of p , we identify several new critical points and regimes for the RSOS model and we initiate the study of the flows between the corresponding field theories.

1. Introduction

The concept of universality in statistical physics states that the field theory describing the continuum limit of a given lattice model is often insensible to the microscopic details of the latter, as long as a suitable set of interaction constants is adjusted so as to place the model at its critical point [1, and references therein]. This issue has been particularly well tested in two dimensions, where many models of interest turn out to be exactly solvable [2]. In particular, the Ising model can be solved on essentially any planar lattice [3], and its ferromagnetic critical point leads in all cases to the same field theory of free Majorana fermions. However,

under very particular circumstances, different, lattice-dependent scaling behaviour can be produced as well. This is the case for fully-frustrated models such as the zero-temperature Ising model on the triangular lattice [4], which gives rise instead to a free bosonic continuum limit [5,6]. Similar remarks can be made about hard lattice gases, which can produce both a universal scaling behaviour of the Lee-Yang type, and other critical points whose continuum limit depends on the underlying lattice structure [7].

It is clearly of interest to investigate the issue of universality in richer and more complicated models, in which adjustable parameters give rise to critical lines along which the critical exponents vary continuously. One case that has been studied in details is that of fully-packed loop models, where the adjustable parameter is the fugacity of a loop. These models have been solved both on the hexagonal [8] and square [9,10] lattices, and the continuum limits turn out to be different. Whilst certainly surprising at first sight, this difference can be traced back to the number of bosonic degrees of freedom of the field theory, which is found to depend on the lattice structure [11], again via a mechanism of full frustration.

The Q -state Potts model [12,13] provides a next natural test bed, containing two adjustable parameters—the number of states Q and the temperature variable $v = e^J - 1$, where J denotes the dimensionless coupling constant—, for which one could hope to see a mixture of universal and non-universal behaviour within one single model. For instance, the Potts models on the square [14] and triangular lattice [15] are both exactly solvable (integrable) at their ferromagnetic phase transition, giving rise to a continuum limit of a twisted free boson, known as the Coulomb gas. On the other hand, both models possess another integrable case—a pair of mutually dual antiferromagnetic (AF) transition curves for the square-lattice model [16], and the zero-temperature AF transition [17,18] (also known as the chromatic polynomial) for the triangular-lattice model—which are both related to continuum theories involving two coupled bosons. These field theories are however profoundly different, the first one involving one compact and one non-compact boson [19], while the second one has been found recently [20] to involve one or two compact bosons depending on the regime (that is, roughly speaking, the range of Q -values).

In order to complete this intricate picture, it seems highly desirable to acquire complete knowledge about the phase diagram and the flow between the various critical points present in each theory. For the square-lattice Potts model we have essentially already a full understanding [19,21]. The goal of the present paper is thus to investigate as far as possible the phase diagram of the triangular-lattice model, and to complete our understanding of its possible types of critical behaviour, outside the particular curves which have already been examined using integrability techniques. To this end, we shall employ a variety of numerical approaches, including the study of limiting curves of partition function zeroes, a recent method involving the roots of a certain graph polynomial, and direct diagonalisation of the transfer matrix (TM). The resulting universality classes will be discussed and classified, when possible, in terms of conformal field theories (CFT) [22].

One feature that is worth special attention is the determination of the AF critical curve.

We shall show here that it bifurcates at a T-point, which in turn accounts for the two distinct regimes that have already been identified in the zero-temperature case [17, 18]. Moreover, we exhibit an unusual phenomenon for $Q > 4$, where pairs of complex-conjugate dominant eigenvalues coexist throughout regions of the (Q, v) phase diagram, rather than just along curves.

The second half of the paper is devoted to a detailed study of the A_{p-1} type RSOS restriction [23–25] of the triangular-lattice Potts model. It is obtained when Q is equal to a Beraha number, $B_p = 4 \cos^2(\pi/p)$ with $p \geq 3$ an integer, and corresponds to the reformulation of the generic Potts model as a restricted height model with local interactions. A previous study of the corresponding square-lattice model for $p = 5, 6, 7$ was reported in [19, figures 23–25]. The plots of the central charge c against the variable $x = v/\sqrt{Q}$ showed interesting new features, including critical points and phases, including some with completely unexpected values of c . We shall see here that the triangular-lattice RSOS model has a very rich phase diagram as well, involving both critical points and critical phases, several of which are absent from the corresponding model on the square lattice. As a first step in their understanding, we provide accurate numerical values of the central charge for these theories.

We have laid out the paper as follows. In section 2 we have included all needed background material to make this paper as self-contained as possible. Section 3 is devoted to explain the main technical tools used in our computations: i.e., the TM approach and the method of critical polynomials (CP). The discussion of our numerical results is contained in section 4, in particular, the position in the (Q, v) -plane of the AF critical curve of the triangular-lattice Q -state Potts model. The next two sections are devoted to the study of the triangular-lattice RSOS model on the torus: in section 5, we focus on the description of this model and its structural properties, while in section 6, we discuss the numerical results we obtain for $4 \leq p \leq 8$. Finally, section 7 deals with the physical implications of our findings and prospects for future work. The amplitudes that appear in the TM method of section 3.1 are collected in Appendix A.

2. Basic setup

2.1. The Q -state Potts model

Let $G = (V, E)$ be an unoriented graph (not necessarily simple) with vertex set V and edge set E , and attach to each vertex $i \in V$ a spin variable $\sigma_i \in \{1, 2, \dots, Q\}$, where $Q \in \mathbb{N}$. The partition function of the Q -state Potts model (in the *spin representation*) then reads

$$Z_G^{\text{Potts}}(Q, J) = \sum_{\{\sigma_i\}} \prod_{\langle i, j \rangle} e^{J \delta_{\sigma_i, \sigma_j}}, \quad (1)$$

where $J = K/T$, the interaction energy between adjacent spins is $-K \delta_{\sigma_i, \sigma_j}$, and T denotes the temperature.

A useful way of rewriting (1) is the so-called *Fortuin–Kasteleyn (FK) representation* [26]:

$$Z_G^{\text{Potts}}(Q, K) = \sum_{A \subseteq E} v^{|A|} Q^{k(A)} \equiv Z_G^{\text{FK}}(Q, v), \quad (2)$$

where $|A|$ is the number of edges in the subset $A \subseteq E$, $k(A)$ denotes the number of connected components in the spanning subgraph (V, A) , and the temperature-like variable v is given by

$$v = e^J - 1. \quad (3)$$

Therefore, the Potts-model partition function is a polynomial in the variables Q, v . This FK representation of the Potts model is useful to make sense of the model when the original variables Q, J are beyond their original physical values: i.e., when Q takes non-integer values and/or the coupling constant J takes imaginary values (i.e., $v < -1$). The usual AF regime corresponds to $v \in [-1, 0)$, while the ferromagnetic one is given by $v \in (0, \infty)$. Furthermore, in the most general setting, one can promote the variables (Q, v) to complex numbers.

There are many studies in the literature that have aimed at elucidating the phase diagram of the Q -state Potts model, mostly in two dimensions. We find mainly two different approaches. The first one is based on the investigation of the zeros of the partition function (2) for recursive strip graphs of the square and triangular lattices with various boundary conditions (see [27, 28] and references therein). The partition function was usually obtained by using TM techniques (see section 3.1). In those studies, the authors considered the partition-function zeros for integer values of $Q \geq 2$ (resp. real values of $v \geq -1$) in the complex v (resp. Q) plane. However, recent studies [29] considered the real zeros of $Z_G(Q, v)$ in the *real* plane (Q, v) . This alternative approach provided useful insights about the phase diagram of the corresponding Potts models.

A more modern approach is based on the use of a CP introduced by two of the present authors [30–34]. This method has provided more precise results on more general families of graphs (see section 3.2).

In Statistical Mechanics one is mainly interested in the behavior of the system when the number of degrees of freedom diverges. Therefore, the main object is not the partition function $Z_G(Q, v)$ (which does not converge to a function in the thermodynamic limit $|V| \rightarrow \infty$), but the *free energy density* (per site):

$$f_G(Q, v) = \frac{1}{|V|} \log Z_G(Q, v). \quad (4)$$

In particular, the thermodynamic limit is taken by choosing a suitable sequence of graphs $G_n = (V_n, E_n)$ converging in some sense to an infinite lattice G_∞ (e.g., one satisfying the van Hove criteria). Then the *infinite-volume free energy* is defined as the limit

$$f_{G_\infty}(Q, v) = \lim_{n \rightarrow \infty} f_{G_n}(Q, v) = \lim_{n \rightarrow \infty} \frac{1}{|V_n|} \log Z_{G_n}(Q, v). \quad (5)$$

Phase transitions then correspond to singularities in v for fixed Q of this limiting function $f_{G_\infty}(Q, v)$.

Remarks. 1. In graph theory the two-variable polynomial $Z_G^{\text{FK}}(Q, v)$ [cf. (2)] is known—after an innocuous change of variables—as the Tutte polynomial [35].

2. In the FK representation one has to be very careful about the thermodynamic limit, as it does not commute with other limits. In particular

$$\lim_{n \rightarrow \infty} \lim_{Q \rightarrow Q_*} f_{G_n}(Q, v) \neq \lim_{Q \rightarrow Q_*} \lim_{n \rightarrow \infty} f_{G_n}(Q, v) \quad (6)$$

for certain values of Q_* . As we will discuss later, these limits do not commute when Q_* is a Beraha number B_p :

$$B_p = 4 \cos^2 \left(\frac{\pi}{p} \right), \quad \text{integer } p \geq 2. \quad (7)$$

3. The infinite-volume free energy (5) does exist and it is a continuous function of v, Q when both parameters belong to their non-degenerate physical ranges (i.e., positive integer Q and $v \in (-1, \infty)$ using the spin representation, or when $Q > 0$ and $v \geq 0$ using the FK representation). In those cases a probabilistic interpretation of the model exists. In other cases, the very existence or uniqueness of the limit (5) is not even clear.

4. It is worth mentioning that studying the real zeros in the real (Q, v) -plane for $v \geq 0$ does not provide any useful information, as there are no *real* partition-function zeros for finite graphs in this range. In this case one has to consider the more “classical” approach of [27, 28, and references therein], or the method of CP to be discussed in section 3.2 below.

2.2. The square lattice

Even though our goal is to complete the phase diagram of the Potts model on the triangular lattice, we need another model where all the important ingredients are exactly known. We will choose the closely related square-lattice Potts model [see figure 1(a)].

Baxter [14, 16] found the exact free energy in the infinite-volume limit (5) along certain curves in the (Q, v) -plane. On these solvable curves, this model becomes integrable. He found four integrable curves (see figure 1(a)): the first two are self-dual [14]

$$v = \pm \sqrt{Q}, \quad (8)$$

and the other two are mutually dual AF curves [16]

$$v_{\pm} = -2 \pm \sqrt{4 - Q}. \quad (9)$$

From the expressions for the bulk free energy $f_{\infty}(Q, v)$ (5) along these curves, one can obtain information about the nature of the phase transitions (when these curves are critical). Baxter found that when moving across the self-dual curves (8) in the v -direction, the system undergoes a first-order (resp. second-order) phase transition when $Q > 4$ (resp. when $0 \leq Q \leq 4$). However, when crossing (9) the transition is simultaneously first *and* second order [19]. Moreover, when moving across $Q = 4$ in the direction along the integrable curves,

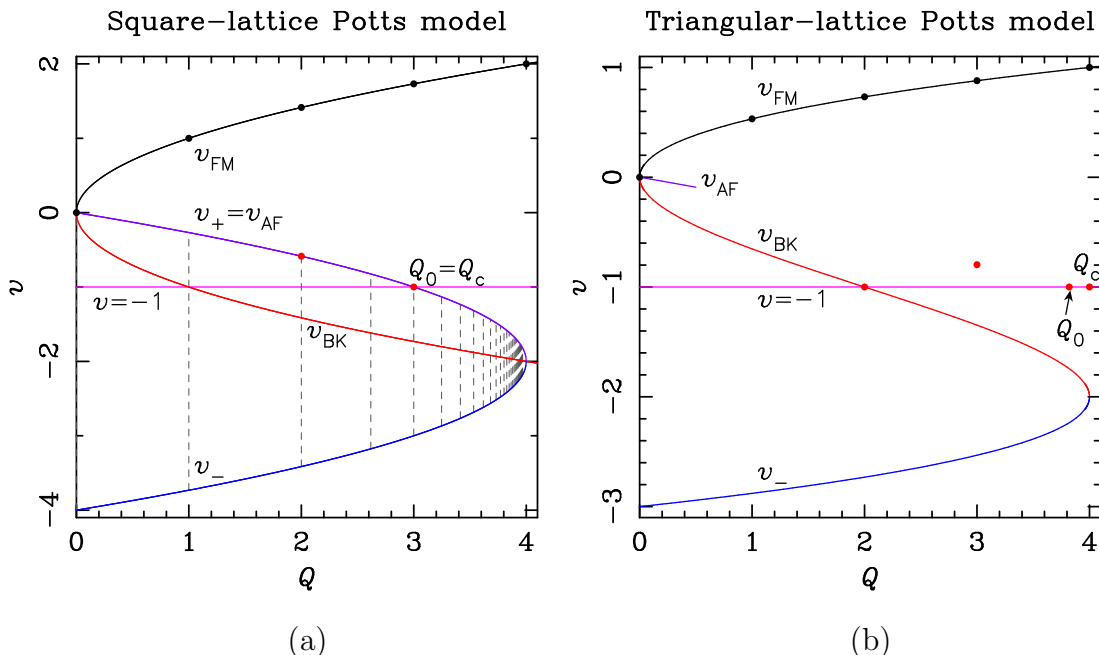


Figure 1. (a) Phase diagram of the square-lattice Q -state Potts model in the real (Q, v) plane. The curve $v_F(8)_+$ is the ferromagnetic critical one, and its analytic continuation $v_{BK}(8)_-$, stays inside the BK phase bounded by the curves (9). The dashed vertical lines within this phase show the location of the first 33 Beraha numbers $B_p(7)$; along these lines the BK phase does not exist. The horizontal (pink) line corresponds to $v = -1$, and the solid dots depict the known critical points for integer values of Q . (b) *Provisional* phase diagram (as based on previous work) of the triangular-lattice Q -state Potts model in the real (Q, v) plane. The three branches of the cubic (12) are expected to play the same role as the curves v_{FM} , v_{BK} , and v_- for the square-lattice model, respectively. The solid thin line emerging from the origin represents the starting values of the expected antiferromagnetic critical curve v_{AF} for this model (see [36]).

the free energy exhibits an essential singularity [2]. There are also singularities in the surface and corner free energies in this case [37, 38].

Within the critical regime $0 \leq Q \leq 4$ much further information can be obtained. Along the integrable curves one can compute various critical exponents, which will typically vary continuously with Q . These exponents provide crucial information that can help identifying the CFT describing the continuum limit. This program has been carried out for the selfdual curves (8), and the corresponding CFT is found to be that of a compactified boson, that can be effectively described by the Coulomb gas (CG) technique [39]. This is arguably the simplest possible CFT with continuously varying exponents.

The coupling constant g of the CG that describes the continuum limit along the selfdual curves (8) is related to the temperature-like parameter v as:

$$v = -2 \cos(\pi g), \quad Q = v^2. \quad (10)$$

This CG coupling constant satisfies $\frac{1}{2} \leq g \leq 1$ for the ferromagnetic branch $v = +\sqrt{Q}$, while

$0 < g \leq \frac{1}{2}$ for the other ('unphysical selfdual' [21]) branch $v = -\sqrt{Q}$. The thermal operator has critical exponent [39, 40]

$$x_T = \frac{3}{2g} - 1 \quad (11)$$

and is conjugate to a perturbation in the temperature variable v around the critical curve (8). In particular, the temperature perturbation is relevant ($x_T \leq 2$) along the upper branch of (8), which is identified with the ferromagnetic critical curve $v_{\text{FM}}(Q) = +\sqrt{Q}$. On the other hand, this temperature perturbation is irrelevant ($x_T > 2$) along the lower branch of (8), which will hence act as a basin of attraction for a finite range of v -values.

This basin is delimited by the AF curves (9) and is called the Berker–Kadanoff (BK) phase [21]. The BK phase is however unphysical, in the sense that all the scaling levels corresponding to the CG description disappear from the spectrum whenever Q is equal to a Beraha number B_p (7) (these numbers are shown in figure 1 as vertical dashed lines). Two distinct representation theoretical mechanisms are responsible for this phenomenon. First, the multiplicity (also known as amplitude, or quantum dimension) of certain eigenvalues of the corresponding TM vanishes at $Q = B_p$, as can be seen from a combinatorial decomposition of the Markov trace [41, 42]. Second, the representation theory of the quantum group $U_{\mathfrak{q}}(sl_2)$ for \mathfrak{q} a root of unity (with $\sqrt{Q} = \mathfrak{q} + \mathfrak{q}^{-1}$) guarantees that other eigenvalues are equal in norm at $Q = B_p$ [21, 25], and as their combined multiplicity is zero, they vanish from the spectrum as well. As a result, for $Q = B_p$ only local observables remain, and these can be realised in an equivalent RSOS height model [43].

Finally, the continuum limit along the curves v_{\pm} (9) that bound the BK phase, gives rise to a more exotic CFT [19, 44] with one compact and one non-compact boson that couple to form the $SL(2, \mathbb{R})/U(1)$ black hole sigma model [45], familiar in the string-theory context [46, 47]. This same continuum limit was recently found to arise also from the seemingly unrelated spin-one Izergin-Korepin loop model on the square lattice [48], which contains as a special case a theta-point collapse transition of lattice polymers [49].

Because the chromatic line $v = -1$ intersects the BK phase in the interval $Q \in [0, 3]$ for the square lattice, and the energy is an irrelevant operator in the BK phase, this scenario can be checked by studying the chromatic zeros in the complex Q -plane along the $v = -1$ line. Detailed studies of these zeros with different boundary conditions (free, cylindrical, cyclic, and toroidal) have been carried out [50–54], and they confirm this scenario (with some minor details that depend on the boundary conditions). In particular, in the thermodynamic limit, chromatic zeros accumulate around certain points (due to the Beraha-Kahane-Weiss (BKW) theorem [55–57]) that are confined to the region $0 \leq Q \leq 3$.

For $Q > 3$ the chromatic line renormalises to infinite temperature ($v = 0$) and is hence non-critical.

Remarks. 1. The lower branch of (8) (i.e., $v_{\text{BK}} = -\sqrt{Q}$) is the analytic continuation of the upper branch of (8), viz., of the critical ferromagnetic curve v_{FM} .

2. The 3-state Potts antiferromagnet on the square lattice is critical on the chromatic

line $v = -1$, but when the temperature is non-zero (i.e., $-1 < v < 0$) it is disordered; so it renormalises to $v = 0$.

2.3. The Berker-Kadanoff phase

The BK phase actually exists on any lattice and governs a finite part of the AF ($v < 0$ and $Q > 0$) part of the phase diagram for the following reasons (see [58]). First, the ferromagnetic transition curve v_F —generalising the upper branch of (8)—must exist on any lattice, by the universality of the CG description with $\frac{1}{2} \leq g \leq 1$. In the (Q, v) -plane this curve must have a vertical tangent at the origin, since the corresponding symplectic fermion CFT (with central charge $c = -2$) is known to describe spanning trees [59]. Indeed, if that tangent was not vertical, we would have instead a spanning-forest model [36], which corresponds to perturbing the free fermion CFT by a four-fermion term [60], which would render it non-critical [60, 61]. This means that the critical curve $Q(v)$ has a vanishing derivative $Q'(0) = 0$ on any lattice.‡ Barring the (unlikely) accident that also $Q''(0) = 0$, we infer that the critical curve continues analytically from the first quadrant $Q, v > 0$ into the fourth quadrant $Q > 0, v < 0$. Invoking again the universal CG description, now with $g < \frac{1}{2}$, we have $x_T > 2$ by (11), and a finite range of v -values will indeed be “controlled” by the BK critical curve v_{BK} . This BK phase is bounded in the (Q, v) plane by two smooth curves v_{\pm} such that for any $Q \in [0, Q_c)$, $0 \geq v_+(Q) > v_-(Q)$. The two curves merge at some value $Q_c > 0$, signaling the termination of the BK phase. The inequality $Q_c \leq 4$ for two-dimensional models follows from quantum group results [21].

The upper curve is usually identified with the critical AF curve, $v_+ = v_{AF}$, and hits the point $(Q, v) = (0, 0)$ at a finite negative slope. This value is related to the critical coupling of the corresponding spanning-forest model [36].

Some unusual features of the BK phase have already been pointed out in the previous section about the square-lattice model, but they hold true for any two-dimensional lattice: At $Q = B_p$, there are vanishing amplitudes and eigenvalue cancellations, so that the actual ground state is deeply buried in the spectrum of the corresponding TM. We now present another related argument, this time directly in the continuum limit, leading to the conclusion that the BK phase should be dismissed as unphysical. The critical behaviour of the BK phase can be obtained by analytic continuation of the CG results for the ferromagnetic transition ($g \geq \frac{1}{2}$). It turns out [62] that some of the critical exponents (namely, magnetic and watermelon exponents) become negative when $g < \frac{1}{2}$. This means that the analytic continuation of the ferromagnetic ground state is not anymore the lowest-energy state in the BK phase, or alternatively, that correlation functions will not decay but rather grow with distance. Such features are clearly unphysical and non-probabilistic.

The existence of the BK phase has been verified for all Archimedean lattices in [31, 32],

‡ This can indeed be checked explicitly for the square and triangular lattices, where the exact critical curve is known; see (8) and (12). Other explicit confirmations for a larger family of lattices, including all the Archimedean ones, have been obtained from the method of CP [32].

and its extent in the (Q, v) plane has been accurately estimated. It was found that in most, but not all [30], cases $Q_c = 4$.

The critical behaviour on the chromatic line $v = -1$ (for general $Q \in \mathbb{R}$) then depends in a crucial way on its intersection with the BK phase. We have seen above that this intersection is the interval $0 \leq Q \leq 3$ for the square lattice. The remainder of the interval $[0, 4]$, namely $3 < Q \leq 4$ in this case, will then have a different behaviour. For the square lattice this behaviour is just non-critical. The triangular lattice however offers a much more interesting alternative, as we shall see presently.

Remark. For non-planar recursive lattices [29], the BK phase is also conjectured to exist, and the value for Q_c might be much greater than 4.

2.4. The triangular lattice

The (Q, v) phase diagram on the triangular lattice appears to be considerably more complicated than was the case on the square lattice. (See figure 1(b) for a graphical summary of the main results known *before* this work.) In particular the part close to $Q = 4$ possesses several intricate features, as witnessed by numerical studies of different types [36, 52, 53, 63]. This model is integrable along the three branches of the cubic [15]

$$v^3 + 3v^2 = Q. \quad (12)$$

Fortunately, the chromatic line

$$v = -1 \quad (13)$$

is also integrable [17, 18] and understanding it in detail should provide valuable information that will also be useful for disentangling the full (Q, v) phase diagram. This programme, initiated in [64], has been completed in [20]: by *exactly* mapping the triangular-lattice Potts AF at zero temperature to a spin-1 integrable vertex model with a suitably chosen twist, whose critical behavior for $Q \in [0, 4]$ has been obtained in terms of CFTs.

Let us parameterise the cubic curve (12) by

$$v = -1 + 2 \cos \left(\frac{2\pi(1-g)}{3} \right), \quad Q = 4 \cos^2(\pi g) \quad (14)$$

where $-\frac{1}{2} \leq g \leq 1$. The range $0 < g \leq 1$ then has the same CG interpretation as for the square lattice: $\frac{1}{2} \leq g \leq 1$ corresponds to v_{FM} , and $0 < g \leq \frac{1}{2}$ to v_{BK} . The interval $-\frac{1}{2} \leq g < 0$ (corresponding to v_-) cannot be interpreted within this CG, but has been shown numerically [19] to belong to the same universality class [44, 45] as the *antiferromagnetic* curve (9) for the square-lattice Potts model (with the same value of Q).

This implies that the middle branch v_{BK} of (12) will control the BK phase, which should extend from the lower branch of (12), that we hence identify with v_- , up to some AF transition curve $v_{\text{AF}} = v_+$, that unfortunately has not yet been determined analytically. In

this work we aim at a precise numerical computation of the antiferromagnetic critical curve, v_{AF} .

This curve cannot be the chromatic line (13), since the latter is not always above the middle branch of (12). At the origin, $(Q, v) = (0, 0)$, the AF curve describes a spanning-forest problem and its slope is known numerically [36]:

$$\left. \frac{dv_{\text{AF}}}{dQ} \right|_{Q=0} = -0.1753 \pm 0.0002. \quad (15)$$

(See the small curve emerging from the origin in figure 1(b).)

Along the chromatic line $v = -1$, Baxter has found [17, 18] three distinct analytic expressions for the TM eigenvalue g_i , whose logarithm is the bulk free energy (per site), and determined the regions of the complex Q -plane where each g_i is dominant. In particular, he found that g_1 corresponds to a non-critical phase which includes the interval $Q \in (-\infty, 0) \cup (4, \infty)$. In this region, exact expressions for the surface and corner free energies are also known [37], and the contributions from corners of angle $\frac{\pi}{3}$ and $\frac{2\pi}{3}$ can even be determined separately [38]. In the limit $Q \rightarrow 4^+$, these corner free energies develop essential singularities that have been determined from the asymptotic analysis of the exact expressions [38].

The BK phase is characterised by g_3 and corresponds to the interval $Q \in (0, Q_0)$ where [18, 63]

$$Q_0 = 3.819\,671\,731\,239\,719 \dots \quad (16)$$

This BK phase is called Regime I in [20]. Finally, g_2 is dominant in the interval $Q \in (Q_0, 4)$, and defines a new critical phase (Regime IV) whose thermodynamic limit is governed by the coset CFT [20]

$$\frac{SU(2)_4 \times SU(2)_{p-6}}{SU(2)_{p-2}}, \quad (17)$$

where p is related to Q by the usual parametrisation $Q = 4 \cos^2(\pi/p)$, and (17) is defined in principle for any integer $p \geq 6$, and by analytic continuation for appropriate real values of p . The central charge for this regime is given by

$$c = 2 - \frac{24}{p(p-4)}, \quad (18)$$

which is the analytic continuation to any real $p > 4$ of that of the S_3 -invariant minimal models studied by Fateev and Zamolodchikov [65, 66]. These models can alternatively be formulated as the above conformal cosets (17). This eigenvalue g_2 describes the colouring problem in this Regime IV; but this also holds for the analytic continuation of g_2 inside the BK phase, at least down to $Q = 2^+$ [20]. It is worth mentioning that in Regime IV the thermal operator is irrelevant, as it is in the BK phase.

Returning now to the phase diagram in the (Q, v) -plane, the simplest scenario that can account for these findings is that the AF transition curve must split at a triple point T into a

branch that goes down to $(Q, v) = (Q_0, -1)$ and delimits the BK phase, and another branch that extends further to the 4-colouring point $(Q, v) = (4, -1)$. This simple scenario is the one we will find as one of the conclusions of this work (see figure 18).

It is also worth mentioning here that the phase diagram for the region $Q > 4$ is not as “simple” as the scenario we have just depicted for $0 \leq Q \leq 4$. Our numerical TM results for strip graphs of finite width $2 \leq L \leq 5$ (displayed in figure 5) show that for $Q > 4$ there are involved structures: many “small” phases (most of them characterised not by a single dominant eigenvalue, but by a pair of complex conjugate eigenvalues), and outward branches for odd values of $L = 3, 5$. These structures can also be seen in figure 8, where the critical-polynomial data is shown. In any case, it is not clear whether these structures converge to anything in the thermodynamic limit. Additional work on larger values of L would be necessary to explore this region of the phase diagram; but this is outside the scope of this paper.

3. Main technical tools

3.1. Transfer-matrix computations on the torus

The construction of the TM for the Q -state Potts model in the FK representation on a triangular-lattice strip with toroidal boundary conditions[§] can be obtained from the general theory developed in detail in [50, 63, and references therein] (in particular, for the chromatic polynomial), the generalisation of the TM formalism for cylindrical boundary conditions and general values of v [28], and the tricks needed to deal with periodic boundary conditions in the longitudinal direction [29, 52, 53, 67]. We will shortly review the main results here to make the paper as self-contained as possible.

First of all, if we want to build the TM for a triangular-lattice strip of width L with periodic boundary conditions in the transverse direction, one has to start from a triangular-lattice strip of width $L + 1$ and free transverse boundary conditions [18, 50]. This is shown in panel (b) of figure 2. Indeed, at the end of the computations, we have to identify this extra column $L + 1$ with column 1.

Secondly, dealing with periodic boundary conditions in the longitudinal direction in the FK representation forces us to keep track of the connectivities among the vertices on the top row $\{1, 2, \dots, L + 1\}$ and those on the bottom row $\{1', 2', \dots, (L + 1)'\}$. Therefore, the TM will act on the space of partitions of the set $\{1', 2', \dots, (L + 1)', 1, 2, \dots, L + 1\}$. Given a partition \mathcal{P} of this set (i.e., a connectivity state $\mathbf{v}_{\mathcal{P}}$), a *link* is a block that contains vertices belonging to both the top and bottom rows. The number of links in a given partition will be denoted by ℓ .

§ We will use the standard notation for boundary conditions of strip graphs: free (resp. toroidal) means that the boundary conditions in both directions are free (resp. periodic). Furthermore, cylindrical (resp. cyclic) means that they are periodic (resp. free) in the transverse direction and free (resp. periodic) in the longitudinal direction.

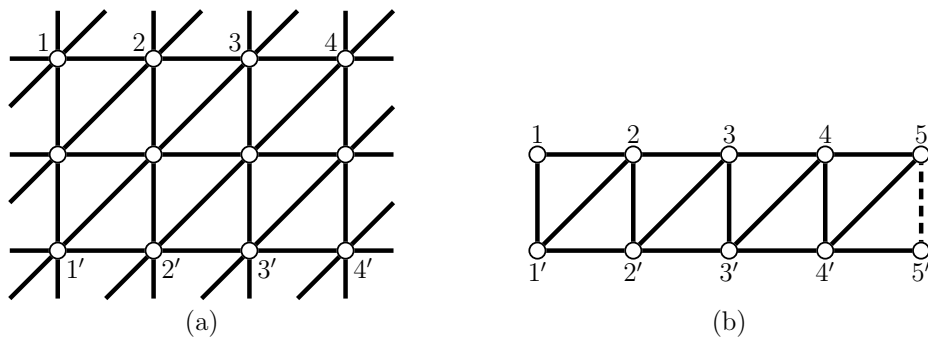


Figure 2. Triangular-lattice on a torus. (a) A triangular-lattice strip on a torus of size 4×3 with periodic boundary conditions. For simplicity, we have represented this strip as a square-lattice strip with oblique edges. The spins on the bottom row (resp. top row) are labeled as $\{1', 2', 3', 4', 5'\}$ (resp. $\{1, 2, 3, 4, 5\}$). The half edges are meant to represent the fully periodic boundary conditions. Notice that we are using an opposite definition of the oblique edges compared to [52, 53]. (b) Transfer-matrix construction for a triangular-lattice strip of width $L = 4$. In this case, we need to start from a triangular-lattice strip of width $L + 1 = 5$ with free transverse boundary conditions. At the end of the computation, we should identify the vertices on the leftmost column with the corresponding ones on the rightmost column (i.e., $1' = 5'$ and $1 = 5$). The rightmost dashed vertical edge is special, as it corresponds to $v = 0$. In this way we ensure that the previous identification gives an edge with the right weight v .

The action of the TM \mathbb{T}_L is to add one layer on top of the strip graph. As usual, we want to write this matrix as a product of “horizontal” and “vertical” operators:

$$\mathbb{Q}_{jk} = \mathbb{1} + v \mathbb{J}_{jk}, \quad (19a)$$

$$\mathbb{P}_j = v \mathbb{1} + \mathbb{D}_j, \quad (19b)$$

where $\mathbb{1}$ is the identity operator, \mathbb{J}_{jk} is a “join” operator that amalgamates the blocks containing the vertices j and k , and \mathbb{D}_j is a “detach” operator that removes vertex j from its block and turns it into a singleton (if j was already a singleton, it provides a factor Q to that term). Then the full TM can be written in a similar way as for the chromatic polynomial [53]:

$$\mathbb{T}_L = \left[\left(\prod_{j=1}^L (\mathbb{P}_j \cdot \mathbb{Q}_{j,j+1}) \right) \cdot \mathbb{P}_{L+1}^{(0)} \right] \cdot \left[\mathbb{J}_{1,L+1} \cdot \left(\prod_{j=1}^L \mathbb{Q}_{j,j+1} \right) \right], \quad (20)$$

where the rightmost operators act first. The first bracket corresponds to the “vertical” TM \mathbb{V}_L , while the second one is related to the “horizontal” TM \mathbb{H}_L , so that $\mathbb{T}_L = \mathbb{V}_L \cdot \mathbb{H}_L$. The oblique edges in the vertical TM corresponds to the operators $\mathbb{Q}_{j,j+1}$ in the \mathbb{V}_L term in (20). The role of the join operators $\mathbb{J}_{1,L+1}$ in the \mathbb{H}_L term is to identify the leftmost and rightmost columns. The operator $\mathbb{P}_j^{(0)} = \mathbb{D}_j$ appearing in the \mathbb{V}_L term is just the evaluation of \mathbb{P}_j at

$v = 0$.|| Its role is to propagate the spin $(L + 1)'$ forwards in time without introducing an extraneous edge weight between spins $(L + 1)'$ and $L + 1$, since this is already taken into account in the first column.

Then the partition function (2) for a triangular-lattice strip graph G of width L and height N on the torus (represented for simplicity by $L_P \times N_P$; see figure 2(a)) is given by the expression:

$$Z_{L_P \times N_P}(Q, v) = \mathbf{u}^T \cdot \mathsf{T}_L^N \cdot \mathbf{v}_{\text{id}}, \quad (21)$$

where the right vector \mathbf{v}_{id} represents the identity connectivity state $\mathbf{v}_{\text{id}} = \{\{1, L + 1, 1', (L + 1)'\}, \{2, 2'\}, \dots, \{L, L'\}\}$ (in other words, we start with the bottom and top rows identified and with the rightmost and leftmost sites in a single block). The left vector \mathbf{u}^T in (21) acts on a connectivity state $\mathbf{v}_{\mathcal{P}}$ as follows:

$$\mathbf{u}^T \cdot \mathbf{v}_{\mathcal{P}} = Q^{|\mathcal{P}'|}, \quad (22)$$

where $|\mathcal{P}'|$ means the number of blocks of the partition \mathcal{P}' , which is related to \mathcal{P} by the equation

$$\mathbf{v}_{\mathcal{P}'} = \mathsf{J}_{1, L+1} \cdot \mathsf{J}_{1', (L+1)'} \cdot \left(\prod_{j=1}^{L+1} \mathsf{J}_{j, j'} \right) \cdot \mathbf{v}_{\mathcal{P}}. \quad (23)$$

In words, \mathbf{u}^T acts on $\mathbf{v}_{\mathcal{P}}$ by identifying the top and bottom rows, and the rightmost vertices $L + 1, (L + 1)'$ with the leftmost ones $1, 1'$, respectively; and then assigning a factor Q to each block of the resulting partition \mathcal{P}' .

Remark. The convention used in this paper to build the triangular lattice (see figure 2) and the corresponding TM (20) are different from those used in previous publications by two of the authors [52, 53]. The only difference is that now the oblique edges point North-East, rather than North-West as in those papers. The final results are of course independent of this choice.

Let us consider a given connectivity state \mathcal{P} as a connectivity state of the bottom (resp. top) row $\mathcal{P}_{\text{bottom}}$ (resp. \mathcal{P}_{top}), and a set of ℓ links. We assume that $1, L + 1$ belong to the same block, as well as $1', (L + 1)'$. As each link connects a single block of the top-row partition to a single block of the bottom-row partition, and vice versa, then $0 \leq \ell \leq L$. See figure 3 for an example. This computation can be simplified by using several simple observations:

- As the TM (20) only acts on the vertices of the top row, T_L has a block-diagonal structure, where each block is characterised by a given bottom-row connectivity. Indeed, all blocks have the same eigenvalues (although in some blocks, these eigenvalues might appear several times). Therefore, it suffices to choose one representative bottom-row

|| In the chromatic-polynomial case, there is no need of introducing the operator $\mathsf{P}_j^{(0)}$, as two edges with $v = -1$ in parallel act like a single edge with the same $v = -1$; but this is not true for a generic value of v . As a matter of fact, two edges in parallel of weights v and v' are equivalent to a single edge with effective weight $v_{\text{eff}} = v + v' + vv'$.

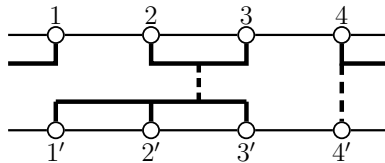


Figure 3. Graphical representation of the connectivity state for a triangular-lattice strip with periodic transverse boundary conditions of width $L = 4$ (once the “extra” vertices $5, 5'$ has been identified with $1, 1'$, respectively). The picture depicts the connectivity state $\mathcal{P} = \{\{1, 4, 4'\}, \{2, 3, 1', 2', 3'\}\}$. This state can be thought of as a bottom-row connectivity $\mathcal{P}_{\text{bottom}} = \{\{1', 2', 3'\}, \{4'\}\}$, a top-row connectivity $\mathcal{P}_{\text{top}} = \{\{1, 4\}, \{2, 3\}\}$, and two links: one connects the first (resp. second) block of $\mathcal{P}_{\text{bottom}}$ with the second (resp. first) block of \mathcal{P}_{top} . The connectivities \mathcal{P}_{top} and $\mathcal{P}_{\text{bottom}}$ are shown as thick solid lines, while the links are depicted as thick dashed lines.

connectivity. But making this choice prevent us of using any additional symmetry in the connectivity space, such as translations along the horizontal direction.

- Neither the detach nor the join operators can increase the number of links of a given connectivity state. Therefore, if we order the connectivity states in a suitable way (i.e., by decreasing number of links), then \mathbb{T}_L takes a block-triangular form. Therefore, its eigenvalues are those of the corresponding diagonal sub-blocks $\mathbb{T}_{L,\ell}$.
- Given the connectivity space generated by a certain bottom-row connectivity and with ℓ links, these objects cannot cross, but move cyclically around the torus. Therefore the relevant symmetry group for the links is the cyclic group C_ℓ . In some sense, toroidal boundary conditions appear to be in the middle of two well-known extreme cases. On one side, we have planar strip graphs with cyclic boundary conditions. In this case, links cannot be permuted at all, and the relevant group is the identity E [41]. On the other hand, for non-planar recursive graphs with periodic longitudinal boundary conditions [67, 68], links can be permuted freely, so the relevant group is the full symmetric group S_ℓ .

The representation theory for the cyclic group C_ℓ [42] implies that the amplitudes associated to each eigenvalue of the block $\mathbb{T}_{L,\ell}$ are certain polynomials in Q . In particular, these amplitudes are the same as for the chromatic-polynomial case [53].

The final goal is to write the Potts-model partition function (2)/(21) on an $L \times N$

triangular-lattice strip graph as a finite sum

$$Z_{L_P \times N_P}(Q, v) = \sum_{\ell=0}^L \sum_{j=1}^{d(L,\ell)} \beta_j^{(\ell)}(Q) \lambda_{\ell,j}(Q, v)^N \quad (24a)$$

$$= \sum_{j=1}^{N_L} \alpha_j(Q) \lambda_j(Q, v)^N. \quad (24b)$$

In (24a), $d(L, \ell)$ is the number of distinct non-zero eigenvalues $\lambda_{\ell,j}$ of the TM block $\mathbb{T}_{L,\ell}$ with the corresponding non-zero amplitudes $\beta_j^{(\ell)}$ given by the representation theory of the group C_ℓ . Notice that there is no reason why a given eigenvalue cannot appear several times within the same block $\mathbb{T}_{L,\ell}$ and/or appear in several blocks simultaneously: e.g., in $\mathbb{T}_{L,\ell}$ and $\mathbb{T}_{L,\ell'}$ with $\ell \neq \ell'$. Then, it is interesting to rewrite the partition function as a “complete” decomposition (24b) in terms of the N_L distinct eigenvalues λ_j appearing in the full TM \mathbb{T}_L with amplitude α_j . These amplitudes should be linear combinations with integer coefficients of the former amplitudes $\beta_j^{(\ell)}$. This form, although not necessary for computing the partition function $Z_{L_P \times N_P}$ and its zeros, it very useful to compute the accumulation points of these zeros as $N \rightarrow \infty$ (e.g., by verifying that the hypotheses of the BKW theorem [55–57] are met).

The number of connectivity states grows exponentially fast with the width of the strip L , so the actual computation of the partition function in the form (24b) could only be achieved for a small number of values of L . However, we could extend our numerical results to larger values of L by using other techniques. These will be explained in section 4.1.

3.2. Critical polynomials

We now discuss a completely different technique for determining the phase diagram: the method of CP. There is now a reasonably large body of work on this [30–34, 69], so we provide only a brief overview here and refer the reader to the literature for details and justification of the method. The first step is to choose a finite graph, which we call the basis, that can be copied and translated to cover the entire lattice. In this case, we choose graphs similar to those we used for the TM computation, namely squares of size $L \times L$. The 4×4 basis is shown in figure 4. The key idea is to compute the weights of two events, $P_{2D}(Q, v)$ and $P_{0D}(Q, v)$, in the FK representation. If we view the basis as embedded in a torus, then $P_{2D}(Q, v)$ is the weight that a cluster wraps both periodic directions, and $P_{0D}(Q, v)$ is the event that there is no wrapping cluster of any kind. The CP for the basis $P_B(Q, v)$ is defined to be

$$P_B(Q, v) \equiv QP_{0D}(Q, v) - P_{2D}(Q, v) \quad (25)$$

and its zeros provide predictions of critical points for arbitrary Q . These predictions are exact for all solved Potts critical thresholds and for unsolved problems they provide accurate estimates that become increasingly so for larger and larger bases. Using extrapolation to

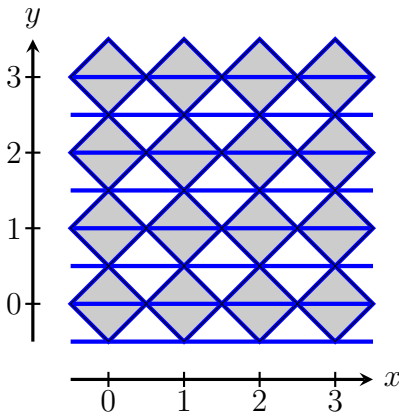


Figure 4. 4×4 basis used to compute the CP on the triangular lattice.

infinite bases, we now have estimates for critical points that far outstrip what can be obtained with Monte Carlo techniques [33]. That $P_B(Q, v)$ is a polynomial of maximum degree $6L^2$ follows from the fact that the basis is a finite graph with $6L^2$ edges.

The way one computes the CP is not important, and a variety of methods have been used in the past [30, 70–73]. But to date, the most efficient technique by far, allowing computation on the largest bases, is to use a TM to find $P_{2D}(Q, v)$ and $P_{0D}(Q, v)$. Recently, one of the authors [33] was able to recast the calculation as an eigenvalue problem, allowing the computation of individual CP roots on semi-infinite lattice strips. However, to get a view of the phase diagram, one really needs to construct the full polynomial $P_B(Q, v)$. Polynomials for all the Archimedean lattices have previously been computed [32] for bases of size up to 5×5 . This was recently extended to 6×6 , using calculations on a supercomputer [34], for all except the triangular lattice, which is done in the present work. In [34], it is described how the algorithm in [32] is parallelised, so the reader is referred to those references for the details.

We ran on Lawrence Livermore National Laboratory’s Cab supercomputer which has 20,736 total cores, each 2.6 GHz with 2GB of RAM. To construct the entire polynomial, one must do the transfer matrix calculation for a variety of Q , and our parallel scheme breaks up the problem so that each processor handles a piece of the vector of connectivity states and a range of Q . The maximum size of the vector is 26,332,020 states and we use 144 Q -values, since the degree in Q of $P_B(Q, v)$ is $4L^2$, the number of vertices in the basis. Our layout of processors can be pictured as an array of $341 \times 12 = 4092$ so that each has 77,220 states and deals with 12 values of Q . The coefficients of the polynomial are very long integers and to construct them we use the Chinese remainder theorem. This means the computation must be done several times modulo a set of prime numbers and in this case we needed 14 primes to get the solution. Each of these calculations required about 7 hours with 4092 processors.

L	$d(L, 0)$	$d(L, 1)$	$d(L, 2)$	$d(L, 3)$	$d(L, 4)$	$d(L, 5)$	N_L
2	2	2	1	0	0	0	5
3	5	10	12	3	0	0	30
4	15	33	55	25	3	0	123
5	52	151 [†]	333 [†]	178 [†]	43	5	586 [†]

Table 1. Distinct non-zero eigenvalues of the TM associated with a triangular-lattice strip graph of width L and toroidal boundary conditions. For each strip graph width $L = 2, 3, 4$, we give the number of distinct non-zero eigenvalues $d(L, \ell)$ of the diagonal block $\mathbb{T}_{L, \ell}$. The number N_L counts the total number of distinct non-zero eigenvalues of the full TM \mathbb{T}_L . This number might be smaller than the sum $\sum_{\ell=0}^L d(L, \ell)$, as some eigenvalues can appear in more than one block $\mathbb{T}_{L, \ell}$. For $L = 5$, the values with the sign [†] are conjectures based on partial factorisation of the corresponding characteristic polynomials and numerical test (see text).

4. Numerical results

4.1. Transfer-matrix results

In this section we will describe the methods we used within the TM approach to obtain the accumulation points of partition-function zeros (i.e., the limiting curves \mathcal{B}_L to be defined below), and extract our estimates for the AF critical curve $v_{\text{AF}}(Q)$.

For the smallest widths $L = 2, 3, 4$ we were able to symbolically compute the TM blocks $\mathbb{T}_{L, \ell}$ for $0 \leq \ell \leq L$, extract all the distinct non-zero eigenvalues λ_j , and compute the corresponding amplitudes $\alpha_i(Q)$. The practical procedure we used can be summarised as follows: Fix a value of L , then

- (i) For each value of ℓ , compute the corresponding diagonal block $\mathbb{T}_{L, \ell}$ of the full TM given a *fixed* bottom-row connectivity (compatible with the value of ℓ) and use all possible top-row connectivity states.
- (ii) For each value of ℓ , compute the characteristic polynomial $\chi_{L, \ell}$ of $\mathbb{T}_{L, \ell}$, and factor it over the integers. Each distinct factor of $\chi_{L, \ell}$ gives distinct eigenvalues $\lambda_{\ell, j}$ [cf. (24a)]. We drop for simplicity those eigenvalues that are identically equal to zero (e.g., for $L = 2$ there is one zero eigenvalue for $\ell = 1$ and another one for $\ell = 2$). The total number of distinct non-zero eigenvalues is the quantity $d(L, \ell)$ shown in table 1. These eigenvalues are algebraic functions of Q and v .
- (iii) Once all the non-zero distinct eigenvalues are computed for all values of ℓ , we only take into account those λ_j that are distinct [cf. (24b)], as we want a “complete” decomposition of the partition function. We finish this part with a list of N_L distinct non-zero eigenvalues λ_j . (See table 1 for the values of N_L .)
- (iv) We know that the amplitudes α_j are linear combinations of the amplitudes $\beta_j^{(\ell)}$ with integer coefficients, and these latter ones are polynomials of degree ℓ in Q [42, 53].

In Appendix A we show which amplitudes do appear in the partition function (24), and in the particular case of the chromatic-polynomial ($v = -1$). Therefore we expect that each eigenvalue λ_j is associated with an amplitude α_j which is a polynomial in Q whose degree is the maximum value of ℓ with which it appears in the spectrum of $\mathbb{T}_{L,\ell}$. Indeed, all eigenvalues coming from the same algebraic equation should have the same amplitude. These amplitudes are fixed by computing the first partition-function polynomials $Z_{L_P \times N_P}(Q, v)$ for small values of $N \geq 1$, and solving the corresponding linear equations.

This procedure has been carried out symbolically using MATHEMATICA for $L = 2, 3, 4$. We have made several cross-checks: a) $Z_{L_P \times N_P} = Z_{N_P \times L_P}$ for any values of L, N ; and b) $Z_{L_P \times N_P}(Q, -1) = P_{L_P \times N_P}(Q)$, where these chromatic polynomials were already computed in [53].

For $L = 5$ this procedure could only be performed successfully in part: for $\ell = 1, 2, 3$ we could find a block structure of the corresponding blocks $\mathbb{T}_{L,\ell}$; but we were unable to symbolically compute the characteristic polynomials $\chi_{L,\ell}$ of the largest sub-block for each of these values of ℓ . (The dimension of these sub-blocks are 126, 240, 135 for $\ell = 1, 2, 3$, respectively.) To ensure that these blocks have non-zero distinct eigenvalues, and that these eigenvalues only appeared in the corresponding blocks, we numerically evaluate all the eigenvalues for several pairs of (Q, v) , and concluded that our conjecture was right. In table 1, these numbers are marked with the superscript \dagger . In this case, we could not obtain the final form for the partition function (24b); but we at least computed all the relevant eigenvalues of \mathbb{T}_5 , and therefore, the corresponding limiting curve \mathcal{B}_5 .

For $6 \leq L \leq 9$, we obtained numerical results for the limiting curve \mathcal{B}_L using a C code. We checked this program by computing these curves for $2 \leq L \leq 5$, and the agreement with the results obtained from the symbolic TM was excellent.

As explained above, for $2 \leq L \leq 4$, we could compute the exact symbolic form for the partition function $Z_{L_P \times N_P}$ (24b). As explained in section 2.1, we look for the zeros of this partition function in the real (Q, v) -plane for $Q \geq 0$ and $v \leq 0$. In order to achieve this goal, we computed the zeros along several lines in this quadrant: $Q = -pv$ with $p = 1, 2, 3$ (the case $p = 1$ essentially corresponds to the flow polynomial [29]), $v = -pQ$ with $p = 1, 2, 3$, and $v = -1, -2, -3, -4$ (the case $v = -1$ is the chromatic polynomial [53]). We have represented in figure 5, for each value of L , these zeros for $N = 19$ (black squares) and $N = 20$ (red open circles). Unfortunately, there are not many zeros along any of these lines.

So far, we have dealt with finite strips, so our results suffer from large finite-size-scaling corrections. Therefore, we should study the thermodynamic limit. As shown in previous papers [27–29, 36, 50–54, 63, 67, 74], a very efficient way to take the thermodynamic limit is the following. We first take the limit $N \rightarrow \infty$, so we have semi-infinite strips with an infinite number of vertices. Then according to the BKW theorem [55–57] (see also [75] for a slight generalisation), the partition-function zeros accumulate around two types of accumulation points:

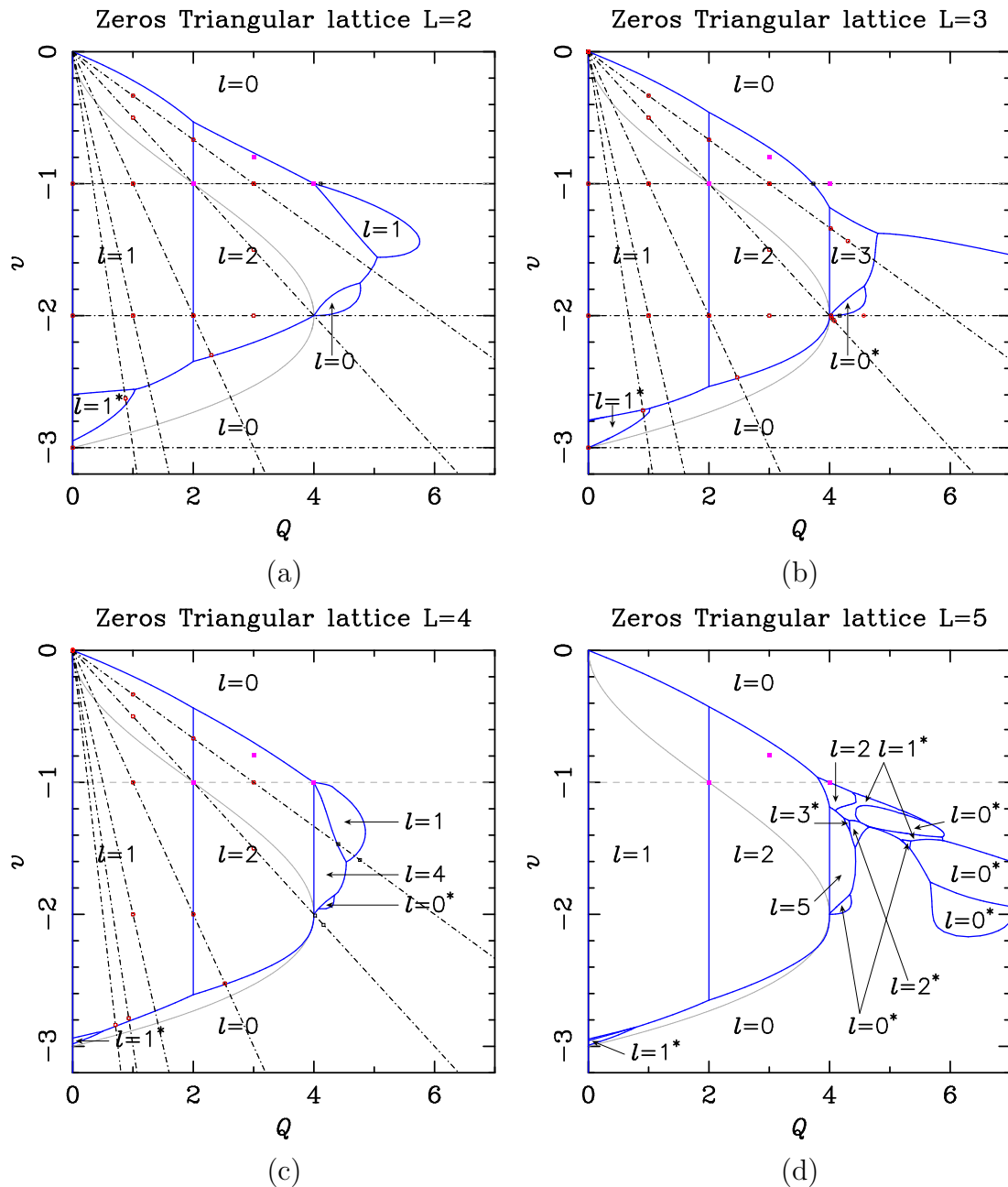


Figure 5. Limiting curves \mathcal{B}_L (solid blue curves) in the real (Q, v) -plane for the Q -state Potts model on triangular-lattice strip graphs embedded in tori of widths $L = 2$ (a), $L = 3$ (b), $L = 4$ (c), and $L = 5$ (d). The solid grey curve corresponds to the two lower branches of the cubic (12). We also show, for each width, the corresponding real zeros for finite strips of length $N = 19$ (black \square) and $N = 20$ (red \circ) along several lines (depicted as dot-dashed lines) of the type $Q = -pv$ ($p = 1, 2, 3$), $v = -pQ$ ($p = 1, 2, 3$), and $v = -1, -2, -3, -4$. The pink full squares (\blacksquare) show the known critical values for $Q = 2, 3, 4$. Each region is labeled with the sector to which the dominant eigenvalue belongs (e.g., $\ell = 1$). An asterisk in the sector label (e.g., $\ell = 1^*$) means that there is a pair of complex-conjugate dominant eigenvalues in that region.

- (i) Isolated limiting points, when there is a single dominant eigenvalue λ_* (with $|\lambda_*| > |\lambda_i|$ for all $i \neq *$), but its amplitude vanishes identically, $\alpha_* = 0$.
- (ii) Limiting curves \mathcal{B}_L formed by points where two or more eigenvalues are dominant in modulus $|\lambda_1| = |\lambda_2| = \dots$. Notice that if all the amplitudes α_k vanish, then we obtain isolated limiting points [75].

By taking this first limit $N \rightarrow \infty$, we can compute both the isolated limiting points and the limiting curves \mathcal{B}_L . If the free energy $f_{L_P \times N_P}$ [cf. (4)] for a finite strip graph of size $L \times N$ is given by

$$f_{L_P \times N_P}(Q, v) = \frac{1}{LN} \log Z_{L_P \times N_P}(Q, v), \quad (26)$$

the corresponding limiting free energy $f_L(Q, v)$ reads

$$f_L(Q, v) = \lim_{N \rightarrow \infty} f_{L_P \times N_P}(Q, v) = \frac{1}{L} \log |\lambda_*(Q, v)|. \quad (27)$$

Therefore, for each value of L we have a “phase diagram” given by the limiting curves \mathcal{B}_L . We empirically know that when the strip graph has periodic longitudinal boundary conditions (as in this case), the corresponding limiting curves bound closed regions [52, 53] (see figure 5). Each of these regions is characterised by the sector to which the leading eigenvalue λ_* belongs. In the chromatic-polynomial case [52, 53] the dominant eigenvalue within each region was unique; but here we find that some (small) regions are characterised by a pair of complex-conjugate eigenvalues. These regions are denoted by a sector label with an asterisk in figure 5.

By inspecting the panels of figure 5 we arrive at the following empirical conclusions:

- The “phase diagram” has two parts. The “regular” one corresponds to the interval $Q \in [0, 4]$, and the relevant sectors are $\ell = 0, 1, 2$. The other piece of the phase diagram corresponds to $Q > 4$, and it contains curves that extend to infinity, and very involved features.
- In the regular part, there is an outer phase characterised by $\ell = 0$, and generically two other phases bounded by two curves. One corresponds to $Q \in [0, 2)$ where $\ell = 1$ is dominant, and the other one corresponds to $Q \in (2, 4)$, where $\ell = 2$ is dominant (for $L \geq 3$). The upper boundary curve $v_{+,L}$ can be interpreted as a finite-size approximation to the AF critical curve v_{AF} , while the lower one $v_{-,L}$ approaches the lower branch of Baxter’s cubic (12) (as one would expect). Notice that for $L = 5$ there is a third phase close to $Q = 4$, where $\ell = 2$ is also dominant. This region can be interpreted as a finite-size approximation to Regime IV. $L = 5$ is the smallest width for which this phase can be directly observed.
- In this regular part, we find three perfectly vertical lines at $Q = 0$, $Q = 2$ and $Q = 4$. These lines are limiting curves. While the lines at $Q = 0, 2$ cover all the points between $v_{\pm,L}$, the one at $Q = 4$ does not in general: this line goes from $v = -2$ to a value $v_1(L) < -1$. See table 2 for our estimates for $2 \leq L \leq 12$.

- The curve $v_{+,L}$ contains a T-point $(Q_T(L), v_T(L))$ for $L = 5, 7, 8$. In these cases, one branch goes from the T-point to $(4, -1)$, and the other one goes to $(4, v_1(L))$. This latter branch crosses the chromatic line $v = -1$ at $Q = Q_2(L)$ (see [53, table 7] for their numerical values). The values of $Q_T(L)$ and $v_T(L)$ are displayed in table 2. The curve $v_{+,L}$ for $L = 2, 3, 4, 6, 9, 12$ does not show such T-point; for $L = 2, 4$ it goes through the point $(4, -1)$; but for $L = 3, 6, 9, 12$ it crosses the line $v = -1$ at a value $Q = Q_0(L)$. The values of $Q_0(L)$ are also displayed in [53, table 7]. From these results and those found on the chromatic line [53], we can conjecture that the curve $v_{+,L}$ contains a T-point and goes through the point $(4, -1)$ for any L not multiple of 3.
- The lines $Q = 1$ and $Q = 3$ can be considered *lines* of isolated limiting points, as the dominant eigenvalues in each of the corresponding regions have amplitudes vanishing at these values. Although this seems to be some sort of contradiction, every point (Q, v) with $v_-(Q) < v < v_+(Q)$ and $Q = 1, 3$ satisfies the conditions of the BKW theorem, and the convergence of the zeros of $P_{L \times N}(Q)$ is exponentially fast in N , rather than algebraically fast as for the ordinary limiting points.
- In the non-regular part of the phase diagram, we find a parity effect: for odd L , there are outward lines going to infinity, while for even L , this part is compact. We also find that for $L \geq 3$ the sector dominant to the right of the vertical line at $Q = 4$ (for $-2 < v < v_1(L)$) is $\ell = L$. Furthermore, we find many regions with dominant complex-conjugate pairs of eigenvalues.

L	$v_1(L)$	$Q_T(L)$	$v_T(L)$
2	-2		
3	-1.1798383409		
4	-1		
5	-1.1862100032	3.7967440229	-0.9606237874
6	-1.245919843		
7	-1.19085474895	3.826(4)	-0.971(2)
8	-1.25306265476	3.772(4)	-0.9541(9)
9	-1.27354		
12	-1.28069		

Table 2. Estimates of the values $v_1(L)$, $Q_T(L)$, and $v_T(L)$ as a function of the width of the triangular-lattice strip graph. The precision of each non-integer entry is of order 10^{-n} , where n is the position of the last quoted digit, unless a larger error is explicitly indicated.

The final goal is to extract information about the true thermodynamic limit from the above finite- L data. We then take the limit $L \rightarrow \infty$, so that the infinite-volume free energy becomes:

$$f(Q, v) = \lim_{L \rightarrow \infty} f_L(Q, v). \quad (28)$$

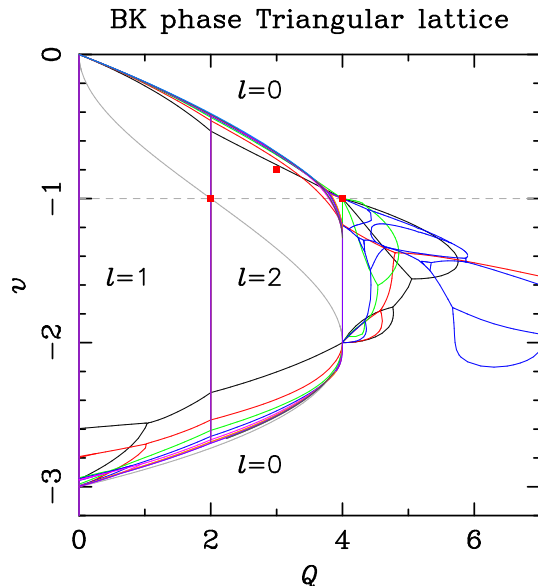


Figure 6. Limiting curves from figure 5 plotted in the same figure. These curves \mathcal{B}_L are depicted as solid lines with colour code $L = 2$ (black), $L = 3$ (red), $L = 4$ (green), $L = 5$ (navy blue), $L = 6$ (pink), $L = 7$ (orange), $L = 8$ (violet), and $L = 9$ (dark grey). The upper blue curve in the range $Q \in [0, 3.6]$ corresponds to the extrapolation of the TM limiting curves. The grey solid curve corresponds to the cubic (12), and the dashed horizontal line, to the chromatic-polynomial subspace ($v = -1$). In each region, we show the dominant link sector. The solid red squares (■) show the known critical points for integer values of $Q = 2, 3, 4$.

In our case, we should try to extract patterns from the above finite-width data. It is interesting to plot together all our limiting curves, at least for the “regular” part of the phase diagram (see figures 6 and 7). The non-regular part of the phase diagram is very involved, with many tiny features, and, as observed above, its structure suffers from large finite-size corrections. Therefore, we refrain from making any further study of this part of the phase diagram, and focus on its regular part.

In figure 6 we show all the limiting curves (or parts of them) for $2 \leq L \leq 9$; they define the full phase diagram. In figure 7(a), we focus on the AF regime $v \in [-1, 0]$ of figure 6, where the physical part of the AF critical curve is expected to be. It is clear from the figure that, at least on the interval $Q \in [0, 3]$, the finite- L estimates for $v_{+,L}$ do not suffer from parity effects and they seem to converge rather quickly to a stable value, that we will identify as the AF critical point v_{AF} . For this reason, we have tried to fit the numerical data to a power-law Ansatz

$$v_{+,L} = v_{\text{AF}} + AL^{-\Delta}, \quad (29)$$

where the Q -dependence has been dropped for simplicity. The fits are rather stable, although the smaller the value of Q the more stable the fit. The estimate for the power increases slowly from $\Delta \approx 1.85$ for $Q = 0.1$ to $\Delta \approx 2.76$ for $Q = 3$. These estimates are depicted in figure 6 as a solid blue curve. If we fit the estimates for the smallest values of Q to a polynomial

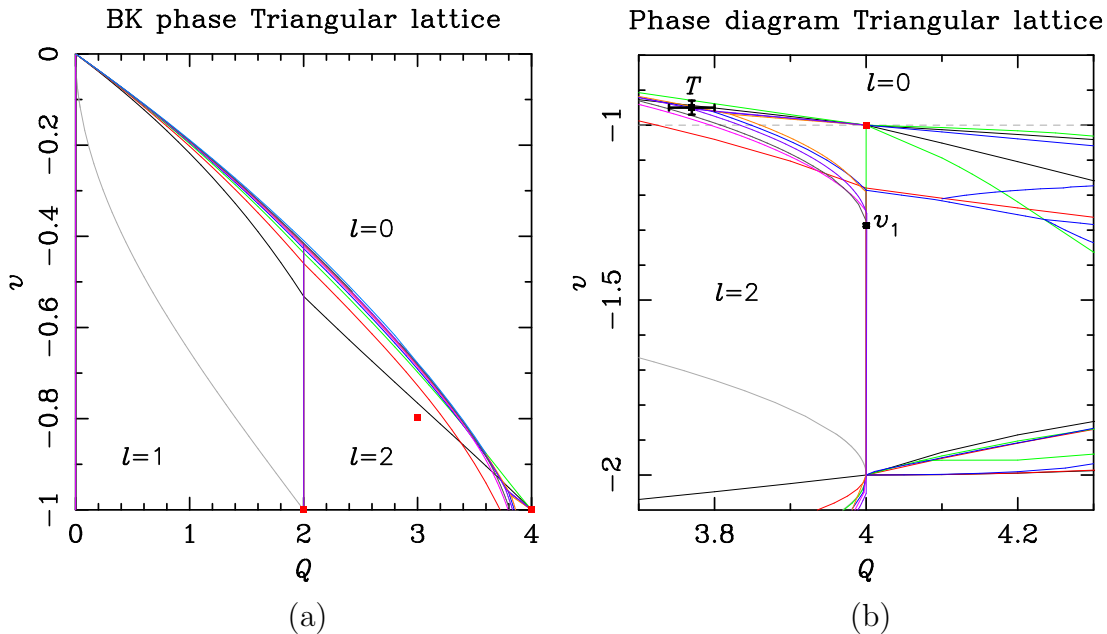


Figure 7. (a) Zoom of figure 6 showing the different approximants to the antiferromagnetic critical curve v_{AF} . (b) Zoom of figure 6 around the line $Q = 4$. The point labeled T is our best estimate for the T-point (Q_T, v_T); and the point labeled v_1 is our best estimate for v_1 . These points are represented by black squares (■). In both panels we use the same symbols and colour codes as in figure 6.

Ansatz, we can obtain a slightly more accurate estimate for the derivative of v_{AF} at $Q = 0$ [cf. (15)]:

$$\left. \frac{dv_{\text{AF}}}{dQ} \right|_{Q=0} = -0.17526 \pm 0.00001. \quad (30)$$

To extend the above results beyond $Q = 3$ and to prevent systematic errors due to parity effects, we have considered the data for $L = 3, 6, 9, 12$ and made a numerical fit to the same Ansatz (29). In this way, we have obtained a reasonably smooth curve $v_{+,L}$ up to $Q \lesssim 3.6$. This is shown in figures 6 and 7(a). Beyond the value $Q \gtrsim 3.6$, we should expect numerical difficulties due to the existence of the T-point T , whose position is given below [cf. (32)].

Our main conclusions are:

- In the region $Q \in [0, 4]$ there is a disordered phase (belonging to the sector $\ell = 0$ when v is close enough to $v = 0$ (= infinite temperature) or v is large enough in modulus and negative (belonging to the unphysical regime).
- There are two boundary curves $v_{\pm,L}$ such that the upper one $v_{+,L}$ (resp. lower one $v_{-,L}$) converges to the AF critical curve v_{AF} (resp. to the lower branch v_- of the cubic (12)). The AF critical curve has a T-point denoted T in figure 7(b), and two branches: one of them, $v_{\text{AF},1}$ goes to the point $(Q_c, v) = (4, -1)$, and the other one, $v_{\text{AF},2}$, to $(Q_0, -1)$,

with Q_0 given by (16), and continues to the point $(4, v_1)$, where

$$v_1 = -1.286 \pm 0.004. \quad (31)$$

This T-point $T = (Q_T, v_T)$ appears for $L = 5$ and $L = 7, 8$. Its approximate position is

$$Q_T = 3.77 \pm 0.03, \quad v_T = -0.95 \pm 0.02. \quad (32)$$

With our current data it is only possible to give rather rough estimates for the error bars in (31)/(32), as these quantities show strong parity effects (mod 3). The above estimates for T and v_1 are displayed in figure 6(b).

- There is a critical phase in the region $Q \in (0, 2)$ and $v_{\text{AF}} < v < v_-$ characterised by the sector $\ell = 1$. This phase has a line of isolated limiting points at $Q = 1$.
- There is a critical phase in the region bounded by the curves v_{AF} for $Q \in (2, Q_T)$, $v_{\text{AF},2}$ for $Q \in (Q_T, 4)$, the line $Q = 4$ for $v \in (-2, v_1)$, the curve v_- for $Q \in (2, 4)$, and the line $Q = 2$ for $v \in (v_-(2), v_{\text{AF}}(2))$. (See figure 7(b) for a graphical representation.) This phase is characterised by the sector with $\ell = 2$, and contains a line of isolated limiting points at $Q = 3$.
- There is another critical phase (corresponding to the regime IV discussed in section 2.4), which is bounded by the point $(4, -1)$, the T point (32), the points $(Q_0, -1)$ [cf. (16)], and the point $(4, v_1)$ [cf. (31)]. This phase might possibly extend to $Q > 4$, but we have not considered this issue here. Finally, we expect that this phase belongs to the sector $\ell = 0$, at least for $L \equiv 0 \pmod{3}$ (see also [53]).

Note that the facts that vertical segments at $Q = 0, 2, 4$ are parts of the limiting curve \mathcal{B}_∞ , and that the vertical segments at $Q = 1, 3$ are lines of isolated limiting points are in full agreement with the conclusions of [67]: the non-negative integers play the same role for non-planar graphs, as the one played by the Beraha numbers for planar graphs. Our results also agree (when restricted to $v = -1$) with those found for the chromatic polynomial of the triangular lattice [53].

4.2. Critical-polynomial results

In figure 8(a), we show the locus of zeros of the CP for $L \times L$ bases with $6L^2$ edges (see figure 4) for $L = 1, 2, \dots, 6$, as well as the simple three-edge basis described in [30]. As in our preceding work [31, 32, 69] the polynomials are available in electronic form as supplementary material to this paper.† Note that the part of the phase diagram which is known exactly, the cubic polynomial (12), is a prediction of the polynomials on every basis. That is, the cubic factors out of every higher-order polynomial. As we increase the size of the basis, the predicted phase diagram becomes more intricate. In particular, vertical rays are clear at the

† This text file `triangular.m` can be processed by MATHEMATICA or—perhaps after minor changes of formatting—by any symbolic computer algebra program of the reader’s liking.

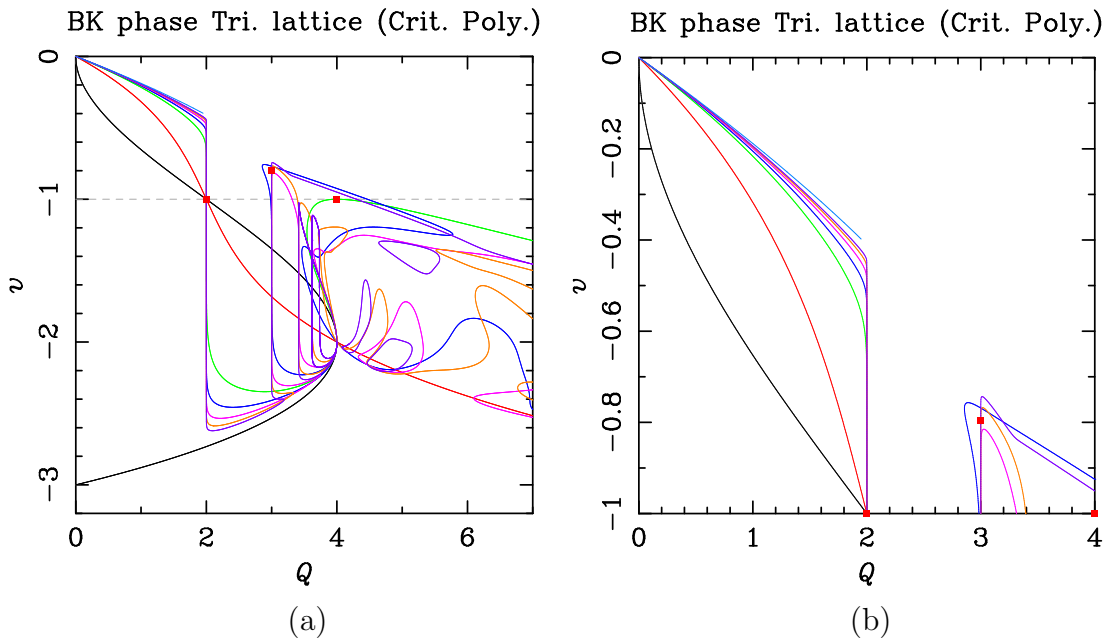


Figure 8. (a) Zeros of the CP for basis size 3 (black), 6 (red), 24 (green), 54 (navy blue), 96 (pink), 150 (orange), and 216 (violet). Notice that the CP for the basis of size 3 is a common factor for the rest of the polynomials, and its zeros coincide with the cubic (12). The upper blue curve in the range $Q \in [0, 1.95]$ corresponds to the extrapolation of the previous curves. The solid red squares (■) show the known critical points for integer values of $Q = 2, 3, 4$. (b) Zoom of the previous panel showing the different approximants to the AF critical curve $v_{AF}(Q)$.

Beraha numbers $Q = B_p$ but apparently only for even p . More of these become visible with increasing L , up to B_{12} for $L = 6$. It therefore seems reasonable to believe that all B_p , for p even, would be present in the limit $L \rightarrow \infty$. For Q not an integer, there is no counterpart of these rays in the partition function zeros. However, as the $p \rightarrow \infty$ limit is reached, the partition function zeros in figure 6 seem to indicate that there is a vertical ray at $Q = 4$, a feature not evident in the CP.

While the picture is fairly clear for $Q < 4$, for $Q \geq 4$ one can discern some features that may be coming into focus, such as a small loop that emerges from the vicinity of $(Q, v) = (4, -2)$, but it generally is not really clear what exactly the CP is predicting in this region. The limiting curves obtained by the TM method seem to provide a more coherent view here, and do include the aforementioned loop, but even so there seems to be more variation between the different values of L than for $Q < 4$.

The AF transition curve v_+ appears to be well converged for $L = 6$, at least where $Q < 2$. This curve is shown in closeup in figure 8(b). The gap in v_+ between $Q = 2$ and $Q = 3$ is possibly an artifact of our choice of basis, and might be filled in by modifying it, perhaps by introducing a twist into the toroidal boundary conditions [30] (although this may introduce gaps elsewhere). The phenomenon of individual bases bringing out certain features of the phase diagram while being blind to others is a common feature of critical polynomials

on Archimedean lattices [34], and is presently not well understood. Nevertheless, comparing figure 8(b) with 6(b) we find very good agreement between the CP prediction of v_+ for $Q < 2$ and the limiting curves computed by the TM method. To be more precise, if we consider the interval $Q \in [0, 1.9]$ in steps of size 10^{-1} , the absolute difference between the TM and CP estimates increases as Q does: it grows from $\approx 9.9 \times 10^{-6}$ at $Q = 0.1$ to 4.5×10^{-4} at $Q = 1.5$, where this difference attains its maximum value. For larger values of $Q \leq 1.9$, this difference becomes somewhat smaller, but is still of order 10^{-4} . We obviously expect identical results of the two methods in the thermodynamical limit.

We also employ the generalisation of the CP method by one of us [33] to bases of size $L \times M$ in the limit $M \rightarrow \infty$. In this approach there is no actual polynomial, but for any given (Q, v) the $M \rightarrow \infty$ limit of each of $P_{2D}(Q, v)$ and $P_{0D}(Q, v)$ in (25) can be related to the largest eigenvalue of a corresponding TM. The value of v is then adjusted by a root-finding algorithm, such as Newton-Raphson or Householder, until $P_B(Q, v) = 0$ to within some tolerance, giving the estimate of the critical point. Once again, the reader is referred to [33] for background details. The main difference here is that the numerical diagonalisation is done using the Arnoldi method as implemented in the ARPACK [76] library, rather than the simpler power method of [33]. This makes it possible to explore the region $3 < Q < 4$, where the power method suffers from severe convergence problems. As we wished to do the calculations in high numerical precision we needed to make major modifications to ARPACK to work with the C++ CLN arbitrary precision library [77]. This required translating the original FORTRAN code of ARPACK into C++ and creating template specialisations to handle CLN numbers.

To find the AF curve, we chose a set of Q values and found the corresponding v satisfying $P_B(Q, v) = 0$ using the above algorithm with an initial guess for v that was close to the data points we had already obtained for this curve. Interestingly, the gap between $Q = 2$ and $Q = 3$ is still present even for these $L \times \infty$ bases. That is, when we choose an initial v near the AF curve for $2 < Q < 3$, the iteration converges only to the cubic curve (12). The AF curve obtained in this way for $0 < Q < 2$ is shown in figure 9(a) for $L = 3, 4, 5, 6$. The curve for $Q > 3$, given in figure 9(b), exhibits a mod 3 parity effect; the computed curves for $L = 3$ and $L = 6$ cross the region uninterrupted by Beraha numbers, much as they do in the 3×3 and 6×6 polynomial curves of figure 8(a). The $L = 4$ and $L = 5$ curves bend downwards, probably on their way to form a vertical ray at some Beraha number as they also do in the polynomial. It thus appears that the results from $L \times \infty$ and $L \times L$ bases are qualitatively very similar. Another feature of both is a ‘‘kink’’ in the $L = 6$ curve around $(Q, v) \approx (3.25, -0.85)$, visible in figure 8(a) and more obvious in 9(a). We hypothesise that 1) this feature will develop further for higher L and converge to the T-point (32), and 2) the CP curve will converge to $v_{AF,1}$ for $Q \in [Q_T, 4]$.

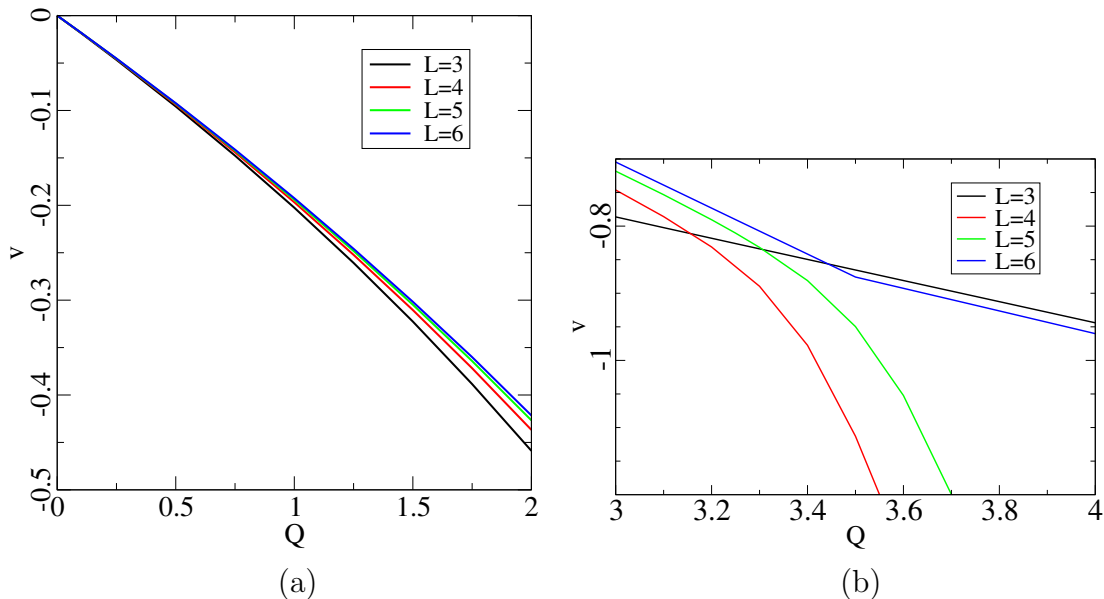


Figure 9. The AF curve calculated using the extension of the CP method to bases of size $L \times \infty$; (a) the region $0 < Q < 2$; (b) the region $3 < Q < 4$. This method gives no information for $2 < Q < 3$.

5. The RSOS model on the torus

There exists another representation of the Q -state Potts model on a planar graph G when Q is a Beraha number B_p (7), namely as an RSOS model of the A_{p-1} type [23–25], where p denotes an integer, such that $p \geq 3$. It is well-known that, if we build the TM for the Q -state Potts model in the FK representation, when evaluated at $Q = B_p$ there are massive eigenvalue and amplitude cancellations, so that the physical ground state is deeply buried in the original spectra. This RSOS representation is very useful in these cases, as it contains only the eigenvalues that do not cancel.

These cancellations imply that the behaviour of the Potts model at Beraha numbers can be quite different from its behaviour at generic values of Q , accessible in the FK representation. In particular, the vertical rays in figures 1 and 8 will turn out to conceal a rich physics, including several interesting critical points and critical phases, once the cancelling eigenvalues have been stripped off via the RSOS construction.

The RSOS model can be defined on any graph embedded in an orientable surface; and in particular on a torus. Therefore, it makes perfect sense to define a RSOS model on a strip graph with toroidal boundary conditions. The equivalence between the RSOS and the Potts models holds true in great generality if the graph is planar, in the sense that if we take appropriate boundary conditions on both models the corresponding partition functions are equal [78–80]. However, this relation is more subtle when the graph is not planar [23, 81, 82]. In this section we will investigate such relation when both models are defined on a torus.

When considering the RSOS model of the A_{p-1} type, it is convenient to use the

temperature variable

$$x = \frac{v}{\sqrt{Q}} \quad (33)$$

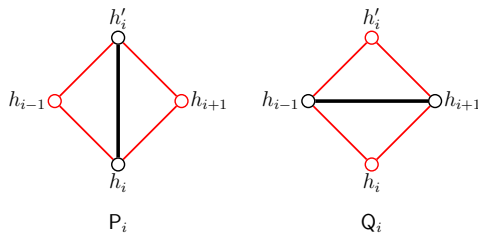
instead of v . It is also useful to define the weights

$$S_h = \frac{\sin(h\pi/p)}{\sin(\pi/p)}. \quad (34)$$

5.1. TM construction for the periodic RSOS model

Let us consider a triangular-lattice strip of width L and periodic transverse boundary conditions. In order to define an RSOS-type model, we need to consider also its dual lattice, which in this case is a hexagonal-lattice strip graph with periodic transverse boundary conditions. (Notice that given a graph embedded in a surface, not necessarily planar, its dual graph is well-defined and it is also embedded in the same surface.) See figure 10.

The variables in the TM formulation of this RSOS model are vectors of dimension $2L$ of the type $(h_1, h_2, \dots, h_{2L})$ such that the odd (resp. even) labeled entries live on the triangular (resp. dual hexagonal) lattice.‡ Periodic boundary conditions mean that $h_{2L+1} = h_1$ and $h_0 = h_{2L}$. The variables h_j , defined for $1 \leq j \leq 2L$, take values in the set $\{1, 2, \dots, p-1\}$, and we shall think of them as “heights”. They are required to satisfy the constraint $|h_j - h_{j+1}| = 1$, which will be extended to any pair of nearest neighbours through the definition of the TM (see below), hence explaining the name Restricted Solid-On-Solid (RSOS) model. The interactions of the RSOS model live on the quadrangular faces; these faces have two vertices of each lattice type in opposite corners. There are two types of interaction terms (we assume that the TM acts upwards; see [82]):



If we have a vector $\mathbf{v} = (h_1, \dots, h_i, \dots, h_{2L})$, then the action of the first of the above operators is the following:

$$\frac{1}{\sqrt{Q}} \mathbf{P}_i \cdot \mathbf{v} = x \mathbf{v} + \delta(h_{i+1}, h_{i-1}) \frac{\sqrt{S_{h_i} S_{h'_i}}}{S_{h_{i-1}}} \mathbf{v}^{(i)}, \quad (35)$$

where x is defined in (33), $\delta(a, b)$ stands for the usual Kronecker delta, the factors S_h are defined in (34), and the vector $\mathbf{v}^{(i)}$ is given by $\mathbf{v}^{(i)} = (h_1, \dots, h'_i, \dots, h_{2L})$. This operator

‡ This parity convention is just one of two possible choices, but we will stick to it hereafter.

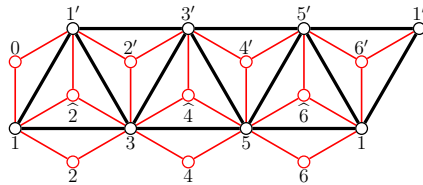


Figure 10. Construction of the TM for a triangular-lattice strip of width $L = 3$ and periodic transverse boundary conditions at $Q = B_p$ with $p \geq 3$. A row of this triangular-lattice strip is depicted with black thick edges and black vertices. We also show the relevant part of the dual strip graph (which is a hexagonal-lattice strip graph with transverse periodic boundary conditions). This dual graph is depicted as thin red lines and red vertices. The RSOS model lives on the vertices of both lattices with interactions around each quadrangular face. In this case, the basis of the space the TM acts on is formed by vectors of the type $(h_1, h_2, \dots, h_{2L})$ where $0 < h_i < p$ and $|h_i - h_{i+1}| = 1$ for each $1 \leq i \leq 2L$ (assuming that $h_{2L+1} = h_1$). The action of TM gives the final vector (h'_1, \dots, h'_{2L}) starting from the initial one (h_1, \dots, h_{2L}) .

propagates a height $h_i \rightarrow h'_i$ standing on a vertex of the original triangular lattice, and it is just another representation of the “vertical” operator P_i in the FK picture based on join/detach operators [50], already discussed in section 3.1. The normalisation on the left-hand side matches the definition (33). Notice also that with the parity convention for indices made above, the operator P_i acts only on odd vertices i in figure 10.

The action of the second operator is

$$\mathbf{Q}_i \cdot \mathbf{v} = \mathbf{v} + x \delta(h_{i+1}, h_{i-1}) \frac{\sqrt{S_{h_i} S_{h'_i}}}{S_{h_{i-1}}} \mathbf{v}^{(i)}. \quad (36)$$

This operator propagates a height $h_i \rightarrow h'_i$ standing on a vertex of the dual hexagonal lattice, and hence, it corresponds to a “horizontal” operator in the FK picture based on join/detach operators [50]. In this case, the operator \mathbf{Q}_i acts only on even sites in figure 10.

We can build the TM in the RSOS representation for a triangular-lattice strip graph with toroidal boundary conditions by going through the following steps: Let us start with a vector $(h_1, h_2, \dots, h_{2L})$, where the variables h_i with $1 \leq i \leq 2L$ satisfy the required constraints; then,

- (i) Build the “horizontal” TM given by $\mathbf{H}_L = \mathbf{Q}_2 \cdot \mathbf{Q}_4 \cdots \mathbf{Q}_{2L} = \prod_{j=1}^L \mathbf{Q}_{2j}$, to obtain the new vector $(h_1, \widehat{h}_2, h_3, \dots, h_{2L-1}, \widehat{h}_{2L})$, where the \widehat{h}_{2j} with $1 \leq j \leq L$ are intermediate variables that we need to keep track of.
- (ii) Insert an extra site which should be neighbour to site 1. The corresponding variable h_0 can take any of the allowed values of $h_0 = h_1 \pm 1$. Then, our vector has been enlarged and takes the form: $(h_0, h_1, \widehat{h}_2, h_3, \dots, h_{2L-1}, \widehat{h}_{2L})$.

- (iii) Build the “vertical” TM given by $V_L = P_1 \cdot Q_2 \cdot P_3 \cdot Q_4 \cdots P_{2L-1} \cdot Q_{2L} = \prod_{j=1}^L (P_{2j-1} \cdot Q_{2j})$, to obtain the new enlarged vector $(h_0, h'_1, h'_2, h'_3, \dots, h'_{2L-1}, h'_{2L})$.
- (iv) If $h_0 = h'_{2L}$, then this vector is valid, so we can drop the first entry and get the final vector $(h'_1, h'_2, \dots, h'_{2L})$ of the right dimension $2L$. If $h_0 \neq h'_{2L}$, then this vector is not valid, and its contribution should be deleted.

Due to the normalisation of the operators P_i [cf. (35)], the transfer matrices in the FK and RSOS representations are now consistently normalised. In more algebraic terms, we can in fact write

$$\frac{1}{\sqrt{Q}} P_i = x \mathbb{1} + E_i, \quad (37a)$$

$$Q_i = \mathbb{1} + x E_i, \quad (37b)$$

where $\mathbb{1}$ is the identity operator, and the E_i are the generators of the Temperley-Lieb (TL) algebra [83] obeying the abstract relations

$$E_i^2 = \sqrt{Q} E_i, \quad (38a)$$

$$E_i E_{i\pm 1} E_i = E_i, \quad (38b)$$

$$E_i E_j = E_j E_i \quad \text{for } |i - j| > 1. \quad (38c)$$

The FK and RSOS expressions given earlier are but two different representations of this abstract algebra. § The dimensions of these representations are not identical, so obviously the spectra of the two TM cannot be identical. There are however many shared eigenvalues, and in particular the “ground state” eigenvalue (i.e., the dominant eigenvalue for $x > 0$, and its analytic continuation for $x < 0$) is identical in both representations. This is of course not enough to ensure the equality of the corresponding partition functions on a finite-size torus. Moreover, each representation does not necessarily admit the same kind of boundary conditions. In particular, it can be shown [84] that taking periodic boundary conditions in the RSOS representation (i.e., taking $h_{i+2L} \equiv h_i$) will produce a superposition of several different (twisted) boundary conditions in the FK representation. We shall admit for the time being that it is of interest to study the RSOS model with periodic boundary conditions, and pursue and clarify some of these subtle aspects below.

In particular, we shall compute the TM in the periodic RSOS representation for several values of $p = 3, 4, 5, 6, 7, 8$; but we will not attempt to compute the full partition function $Z_{L_P \times N_P}^{\text{RSOS}}$. Therefore, our comparison will be made at the level of eigenvalues (or free energies). We stress again that the above normalisation allows the direct comparison among eigenvalues in different representations of the TL algebra. In particular, we shall compare the RSOS representation with the FK representation for integer $p \geq 3$, and with the Potts spin representation for integer $Q = 2, 3$ (hence $p = 4, 6$).

§ In the case of periodic boundary conditions, all indices i are considered mod $2L$. In addition, (38) must be supplemented by further relations to make the algebra finite-dimensional, giving rise to the so-called affine TL algebra. We refer to [84] for further discussion.

5.2. Symmetries and sector decomposition

If we consider the RSOS model described above, we can try to use the full configuration space for moderate values of L . However, since its dimension grows exponentially fast with L , it is also of interest to diminish its size using lattice and target space symmetries. To this end, we first observe that given a configuration vector $(h_1, h_2, \dots, h_{2L})$, it is obvious from the definition of \mathbf{P}_i and \mathbf{Q}_i that the height variables h_i having labels i of the same parity will take values with the same parity. This condition is preserved under the action of the full TM. Therefore, we can define two sectors:

- **Even sector:** the heights on the triangular lattice take even values (and those on the dual hexagonal lattice take odd values). This means that the odd (resp. even) entries of the state vector $(h_1, h_2, \dots, h_{2L})$ take even (resp. odd) values: e.g., $(2, 1, 2, 3, 4, 3)$ for $L = 3$. The transfer matrix computed on this sector will be denoted by $\mathbb{T}_{\text{RSOS}}^{(\text{even})}$.
- **Odd sector:** the heights on the triangular lattice take odd values (and those on the dual hexagonal lattice take even values). This means that the odd (resp. even) entries of the state vector $(h_1, h_2, \dots, h_{2L})$ take odd (resp. even) values: e.g., $(1, 2, 3, 4, 3, 2)$ for $L = 3$. The transfer matrix computed on this sector will be denoted by $\mathbb{T}_{\text{RSOS}}^{(\text{odd})}$.

The RSOS model with periodic transverse boundary conditions has two symmetries that might help to reduce the size of the configuration space:

- **Spin-reversal symmetry:** the RSOS partition function is invariant under the transformation $h_k \rightarrow p - h_k$ for $0 \leq k \leq 2L$. If we denote by \mathbf{v}' the vector obtained from \mathbf{v} by applying the latter transformation, we can make a change from the initial basis $\mathcal{B} = \{\mathbf{v}_j, \mathbf{v}'_j\}$ to $\mathcal{B}' = \{\mathbf{v}_j + \mathbf{v}'_j, \mathbf{v}_j - \mathbf{v}'_j\}$. Indeed, the spectra of the corresponding transfer matrices should coincide. We can now use the subspace of those states that are invariant under spin reversal $\mathcal{B}'' = \{\mathbf{v}_j + \mathbf{v}'_j\}$, and build the corresponding transfer matrix $\mathbb{T}_{\text{RSOS}}^{(\text{S})}$ on it. We can do the same procedure on the even and odd sectors defined above. || The corresponding transfer matrices are denoted $\mathbb{T}_{\text{RSOS}}^{(\text{even}, \text{S})}$ and $\mathbb{T}_{\text{RSOS}}^{(\text{odd}, \text{S})}$.
- **Rotational symmetry:** due to the periodic boundary conditions in the transverse direction, the RSOS partition function should be invariant under any translation along that direction. Note that, since the odd (resp. even) entries in a state vector correspond to vertices on the triangular (resp. dual hexagonal) sublattices, these translations should be done in steps of two units. Instead of building a basis that is merely invariant under rotations, we consider a basis that is invariant under both rotation *and* spin-reversal symmetries: now each element of the basis contains a given state, its spin-reversal counterpart, and all those vectors obtained from the previous ones by translations of even length. The corresponding transfer matrix will be denoted by $\mathbb{T}_{\text{RSOS}}^{(\text{F})}$. (The superscript F stands for ‘‘Fully symmetric’’.) If we perform the same procedure on each of the two even/odd sectors for even values of p we obtain transfer matrices that we denote $\mathbb{T}_{\text{RSOS}}^{(\text{even}, \text{F})}$ and $\mathbb{T}_{\text{RSOS}}^{(\text{odd}, \text{F})}$.

|| This can only be done for even values of p . For odd values of p , \mathbf{v}_j and \mathbf{v}'_j belong to distinct sectors.

Finally, we have implemented the construction of these TM in two independent ways: a) a symbolic approach using MATHEMATICA (similar to the one used in section 4.1); and b) a numerical approach using code written in C and using Arnoldi's algorithm. Indeed, we have cross-checked the results for the smaller values of L , and the agreement is perfect (within the precision of the corresponding numerical procedures).

5.3. Dimension of the TM

The dimension of the TM in the FK representation is independent of Q , but depends on the width L and on the boundary conditions. For periodic boundary conditions in the longitudinal direction, the TM can be decomposed in sectors corresponding to the number $\ell = 0, 1, \dots, L$ of marked clusters that propagate along the time direction. Each sector can be equivalently realised, for $\ell \geq 1$, as a standard module in the representation theory of the affine TL algebra, and as an appropriate quotient for $\ell = 0$. The dimensions d_ℓ^{FK} read

$$d_0^{\text{FK}} = \frac{1}{L+1} \binom{2L}{L}, \quad d_\ell^{\text{FK}} = \binom{2L}{L-\ell} \quad \text{for } 1 \leq \ell \leq L. \quad (39)$$

The dimension of the TM in the RSOS representation can be inferred from the number of paths M_{ba} on the Dynkin diagram A_{p-1} , going from node $h_0 = a$ to node $h_{2L} = b$ in precisely $2L$ steps. This is given by [24, eq. (4.17)]

$$M_{ba} = \frac{2}{p} \sum_{j=1}^{p-1} \sin\left(\frac{\pi a j}{p}\right) \sin\left(\frac{\pi b j}{p}\right) \left[2 \cos\left(\frac{\pi j}{p}\right)\right]^{2L}. \quad (40)$$

To have periodic boundary conditions we must impose $h_{2L} = h_0$. It follows that

$$\dim \mathbb{T}_{\text{RSOS}}^{(\text{even})} = \dim \mathbb{T}_{\text{RSOS}}^{(\text{odd})} = \frac{1}{2} \sum_{a=1}^p M_{aa}. \quad (41)$$

These dimensions of course depend explicitly on p .

5.4. Boundary conditions

It was mentioned towards the end of section 5.1 that the periodic boundary condition imposed on the RSOS model corresponds to a superposition of several boundary conditions in the RSOS model. We now review this construction in sufficient details to be able to correctly interpret the results that will be given in section 6.

Consider the space \mathcal{W}_a of RSOS states $(h_0, h_1, \dots, h_{2L})$ in which the first and last heights have been constrained to take equal values, $h_0 = h_{2L} = a$, where $a \in \{1, 2, \dots, p-1\}$ is fixed. The space \mathcal{W}_a has dimension M_{aa} given by (40). Within \mathcal{W}_a we now consider the *non-periodic* TL algebra in the RSOS representation, with generators $\{\mathbf{E}_i\}_{i=1}^{2L-1}$. Combining the concepts of braid translation and blobbed boundary conditions, one may manufacture another operator \mathbf{E}_0 (it is given by an explicit, albeit highly non-local, expression in terms

of the non-periodic generators E_i) so that the set $\{E_i\}_{i=0}^{2L-1}$ obeys the algebraic relations of the *periodic* TL algebra [84]. Any operator \mathcal{O} within the periodic TL algebra can now be replaced by a corresponding expression $\tilde{\mathcal{O}}_a$ in the non-periodic one, by using E_0 as the periodic generator; we shall refer to this procedure as “periodicisation”. In particular, one might periodicise the TM of the triangular-lattice Potts model, by exploiting its expression in terms of the TL generators and using the RSOS representation for the latter, as given in section 5.1.

It turns out that the union over a of the spectra of each periodicised operator $\tilde{\mathcal{O}}_a$ is equal to the spectrum of the original operator \mathcal{O} in the genuine periodic RSOS representation. Moreover, the parameter a can be interpreted as a certain twist which amounts, in the corresponding loop model representation of the TL algebra, to giving the weight

$$n_a = 2 \cos \left(\frac{\pi a}{p} \right) \quad (42)$$

to each loop that wraps around the periodic direction (i.e., a loop which is non-homotopic to a point). Alternatively, in the FK cluster representation, each wrapping cluster will get the weight $Q_a = n_a^2$ because it is surrounded by a pair of wrapping loops; notice in particular that the sign of n_a is immaterial. The case $a = 1$ thus gives rise to $Q_a = Q$, meaning that wrapping clusters get the same weight as non-wrapping ones—in other words, this reproduces the effect of periodic boundary conditions in the FK representation.

Summarising, the periodic RSOS representation can be decomposed into several sectors a , of which $a = 1$ corresponds to periodic boundary conditions in the corresponding FK model, whereas other values of a are equivalent to giving a modified weight $Q_a = n_a^2$ to wrapping clusters. We shall use this result below to analyse the TM \mathbb{T}_{RSOS} in the periodic RSOS representation. However, we shall make no attempt on constructing the operators $(\tilde{\mathbb{T}}_{\text{RSOS}})_a$ for each sector a individually.

6. Numerical results for the RSOS model on the torus

In this section we discuss our numerical results for the RSOS model of type A_{p-1} for $3 \leq p \leq 8$ on a triangular-lattice strip graph with toroidal boundary conditions. We shall consider only strips of widths that are a multiple of 3: i.e., $L = 3, 6, 9, 12, 15$, in order to avoid the mod 3 parity effects which we have observed above in both the limiting curves and the roots of the CP. Because the computations for $L \geq 12$ are very demanding, we will focus in this case (except for $p = 4$) on the even RSOS sector with all symmetries taken into account (i.e., the spectra of $\mathbb{T}_{\text{RSOS}}^{(\text{even}, \text{F})}$).

We first consider, in section 6.1, the values $p = 3, 4, 6$ for which $Q = B_p$ is an integer. In these cases, we have three representations of the corresponding Q -state Potts model: i.e., the spin, FK, and RSOS representations. Next, in section 6.2, we will consider the cases $p = 5, 7, 8$ for which Q is non-integer. In these cases, only the FK and the RSOS representations are available.

For each fixed value of p , we will study in detail the corresponding RSOS model by considering the different sectors and symmetries described in section 5.2; the main focus will be on the even and odd RSOS sectors with all symmetries taken into account (i.e., $\mathbb{T}_{\text{RSOS}}^{(\text{even},\text{F})}$ and $\mathbb{T}_{\text{RSOS}}^{(\text{odd},\text{F})}$). We will compare the resulting RSOS spectra with the eigenvalue structure of the spin [50, and references therein] and FK representations of the associated Q -state Potts model (with $Q = B_p$). Our goal will be to find, for each p , values of the variable x for which the RSOS model displays new physical properties.

In particular, we aim at identifying critical points and critical phases. This is most easily done by computing the effective central charge c from the finite-size corrections to the free energy. In some cases c can be identified with that of a known CFT, and so the whole operator content is fixed by inference. In other cases the identification is ambiguous or uncertain, due to an insufficient numerical precision or the lack of an obvious candidate CFT. In those cases we content ourselves by determining a numerical value of c , and we leave the precise identification of the operator content for future work.

Two known CFT will play a special role below. The first one is the usual unitary minimal model of central charge

$$c_{\text{FM}} = 1 - \frac{6}{p(p-1)}. \quad (43)$$

As indicated by the subscript, this CFT is expected to be related with the ferromagnetic (FM) transition in the Potts model. The other one is the $sl(2, \mathbb{R})/u(1)$ Euclidean black hole sigma model with

$$c_{\text{PF}} = 2 - \frac{6}{p}, \quad (44)$$

which is the continuum limit of the AF transition in the square-lattice Potts model [19,44,45]. Numerical evidence has previously been given in [19, figure 27] that this theory also describes, for real $p \in [2, \infty)$, the transition at $v_-(Q)$ of the triangular-lattice model in the FK representation. We shall see here that the restriction of this theory to integer $p \geq 3$ —that is, the $sl(2)/u(1)$ parafermion CFT, still with central charge (44)—will account as well for the behaviour of the RSOS model at $v_-(Q)$. The subscript PF in (44) is chosen to remind us about this connection with parafermions.

6.1. Results for integer Q

We have made two independent cross-checks to ensure the correctness of our numerical techniques.

The first one is to reproduce the trivial result for $Q = 1$ ($p = 3$): the TM in the RSOS representation has a unique eigenvalue $\mu = (1+x)^{3L} = (1+v)^{3L}$. This is indeed the expected result, as the partition function for a triangular-lattice strip on a torus of dimensions $L \times N$ is $Z_G^{\text{Potts}}(1, v) = (1+v)^{3LN}$. We have also computed the free energy (27) of a triangular-lattice Q -state Potts model on the torus of width $L = 3$ for $Q = 2, 3$ using the TM in the

spin representation. These free energies coincide (within the numerical precision) with those obtained using the TM in the FK representation when taking into account the vanishing amplitudes and the eigenvalue cancellations. Notice that in these three cases $Q = 1, 2, 3$, we do find such vanishing/cancellation features in the FK amplitudes/eigenvalues.

6.1.1. $Q = B_4 = 2$. We show the dimensions of the TM in the spin, FK, and RSOS representations in table 3. For $p = 4$, we see that $\dim \mathsf{T}_{\text{spin}} = \dim \mathsf{T}_{\text{RSOS}}^{(\text{even})} = \dim \mathsf{T}_{\text{RSOS}}^{(\text{odd})}$ for all widths L . This equality can be interpreted as follows: the RSOS variables on one sublattice all take the value 2, while those on the other sublattice can take the other two possible values 1, 3. Hence, there is a bijection between RSOS configurations in the even or odd sectors, and Ising configurations on one sublattice.

The dimensions of $\mathsf{T}_{\text{RSOS}}^{(\text{even})}$ and $\mathsf{T}_{\text{RSOS}}^{(\text{odd})}$ of course also agree with (41), when the sum is constrained to the specified parity of a .

p	L	$\dim \mathsf{T}_{\text{FK}}$	$\dim \mathsf{T}_{\text{spin}}$	$\dim \mathsf{T}_{\text{RSOS}}^{(\text{even})}$	$\dim \mathsf{T}_{\text{RSOS}}^{(\text{even},\text{F})}$
4	3	30	8	8	2
	6		64	64	8
	9		512	512	30
	12		4096	4096	180
6	3	30	27	28	6
	6		729	730	68
	9		19683	19684	1098
	12			531442	

Table 3. Dimension of the TM for the Potts model with $Q = B_p$ ($p = 4, 6$) on a triangular-lattice strip graph on the torus in the FK representation T_{FK} , in the spin representation T_{spin} , and in the RSOS representation in the *even* sector $\mathsf{T}_{\text{RSOS}}^{(\text{even})}$, and in the same sector with all symmetries $\mathsf{T}_{\text{RSOS}}^{(\text{even},\text{F})}$. Note that $\dim \mathsf{T}_{\text{RSOS}}^{(\text{even})} = \dim \mathsf{T}_{\text{RSOS}}^{(\text{odd})} = \dim \mathsf{T}_{\text{RSOS}}^{(\text{S})} = 2 \dim \mathsf{T}_{\text{RSOS}}^{(\text{even},\text{S})} = 2 \dim \mathsf{T}_{\text{RSOS}}^{(\text{odd},\text{S})}$, and $\dim \mathsf{T}_{\text{RSOS}}^{(\text{F})} = 2 \dim \mathsf{T}_{\text{RSOS}}^{(\text{odd},\text{F})} = 2 \dim \mathsf{T}_{\text{RSOS}}^{(\text{even},\text{F})}$.

The free energy (per site) for a given sector of the RSOS model is expressed in terms of the dominant eigenvalue μ_* of the corresponding TM by the analogue of (27). For each pair $(p, L) = (4, L)$ with $L = 3, 6, 9, 12$, we have computed the free energy for each RSOS sector $f_L^{(\text{RSOS})}(p, x)$ in the interval $x \in [-3, 1]$ in steps of 10^{-2} . We can compare these free energies with those of the corresponding Q -state Potts model with periodic boundary conditions in the spin representation, $f_L^{(\text{spin})}(Q, v)$, with $Q = B_p = 2$, and $v = x\sqrt{B_p}$.

According to section 5.4, the quantities $f_L^{(\text{RSOS})}(p, x)$ and $f_L^{(\text{spin})}(Q, v)$ need not agree for any value of x . Indeed, the former quantity contains two different boundary conditions, corresponding to giving the weight $Q_1 = 2$ or $Q_2 = 0$ to each wrapping cluster. These

can be identified with, respectively, periodic ($a = 1$) and antiperiodic ($a = 2$) boundary conditions for the Ising spins, where the label a has the same meaning as in (42). For $x > 0$, the periodic boundary condition is dominant by probabilistic reasons, implying that $f_L^{(\text{RSOS})}(p, x) = f_L^{(\text{spin})}(Q, v)$ indeed, but this equality might not hold true for any $x < 0$.

To give a quantitative measure of the difference between these two free energies, we introduce the quantity

$$\Delta_f(p, L) = \max_{x \in [-3, 1]} \left| f_L^{(\text{spin})}(B_p, v) - f_L^{(\text{RSOS})}(p, x) \right|. \quad (45)$$

In table 4 we show this quantity for each pair $(p, L) = (4, L)$ and each RSOS model we have studied.

p	L	RSOS (even)	RSOS (odd)	RSOS (even,S)	RSOS (odd,S)	RSOS (S)	RSOS (even,F)	RSOS (odd,F)	RSOS (F)
4	3	$3 \cdot 10^{-4}$	0	0	0	0	0	0	0
	6	10^{-5}	0	0	0	0	0	0	0
	9	10^{-6}					0	0	0
	12	10^{-7}							0
6	3	$6 \cdot 10^{-2}$	$6 \cdot 10^{-2}$	$4 \cdot 10^{-4}$	0	$4 \cdot 10^{-4}$	$8 \cdot 10^{-2}$	$8 \cdot 10^{-2}$	$8 \cdot 10^{-2}$
	6	$9 \cdot 10^{-6}$	$6 \cdot 10^{-6}$	$9 \cdot 10^{-6}$	0	$9 \cdot 10^{-6}$	$9 \cdot 10^{-6}$	0	$9 \cdot 10^{-6}$
	9	$6 \cdot 10^{-3}$					$3 \cdot 10^{-2}$	$3 \cdot 10^{-2}$	

Table 4. Difference $\Delta_f(p, L)$ (45) between the free energy obtained in the periodic spin representation for $Q = 2, 3$, and the free energy computed for the different sectors of the periodic RSOS model with $p = 4, 6$, respectively.

As expected from the bijection between states in the RSOS and spin representation, we find that for *all* (but one) sectors of the RSOS model, the free energy $f_L^{(\text{RSOS})}$ coincides exactly with $f_L^{(\text{spin})}$.

The single exception to this generic behaviour is the free energy coming from the even sector of the RSOS model (i.e., $\mathbb{T}_{\text{RSOS}}^{(\text{even})}$). Notice that the configuration space in this RSOS sector is equivalent to that of an Ising model on the dual hexagonal sublattice, and no symmetry has been taken into account in both models. In any case, the RSOS free energy in this sector differs slightly from the one computed in the spin representation, and the difference $\Delta_f(4, L)$ decreases with L . Roughly speaking, as L increases by 3 units, the difference decreases by one order of magnitude. (See figure 11(a) and table 4.) It is worth mentioning that $f_L^{(\text{spin})}$ and $f_L^{(\text{RSOS, even})}$ differ precisely at values of x where the model is not critical, as it is clear from figure 11.

We can go further and compare the full spectra of these various transfer matrices. We find that

$$\text{sp } \mathbb{T}_L^{(\text{RSOS})}(x) \subset \bigcup_{a=1,2} \text{sp } \mathbb{T}_L^{(\text{spin}, a)}(x), \quad (46)$$

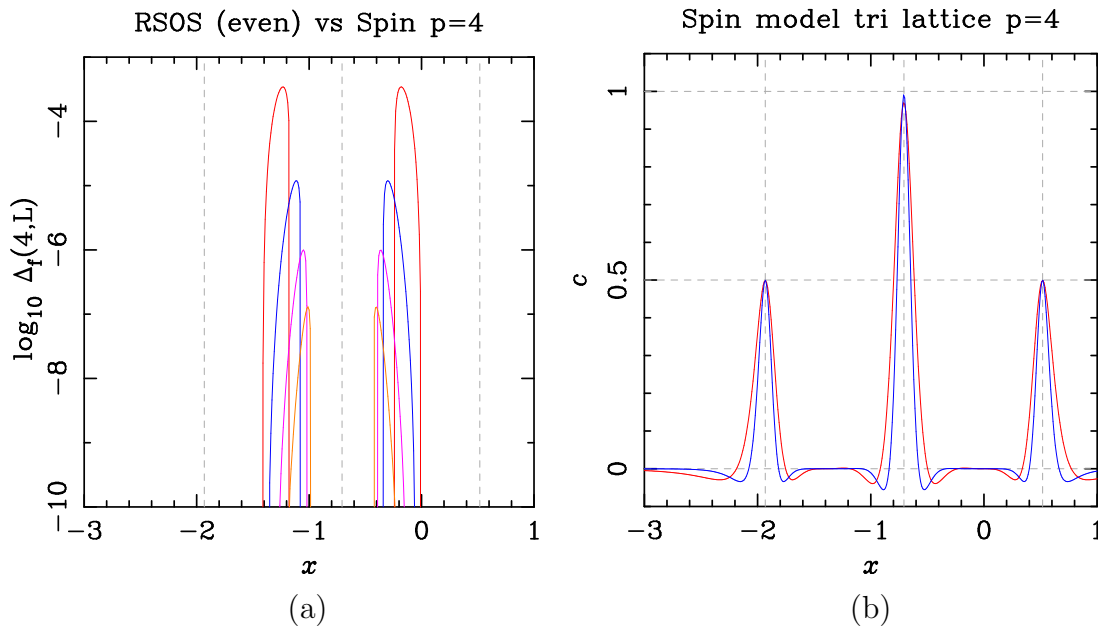


Figure 11. Free energy and central charge for the Ising model on a triangular lattice with toroidal boundary conditions and widths $L \equiv 0 \pmod{3}$ in the RSOS representation. (a) Absolute difference $\Delta_f(4, L)$ [cf. (45)] between $f_L^{(\text{spin})}$ and the free energy $f_L^{(\text{RSOS, even})}$ of the even sector of the RSOS model. (For the other RSOS sectors $\Delta_f(4, L) = 0$.) We show the data for widths $L = 3$ (red), $L = 6$ (blue), $L = 9$ (pink), and $L = 12$ (orange). (b) Central charge obtained from the Ansatz (47). We display the results for $L_{\min} = 3$ (red) and $L_{\min} = 6$ (blue). The vertical dashed grey lines in both panels show the roots of Baxter's cubic (12), and the horizontal lines in (b) mark the expected results $c = 1/2$ and $c = 1$.

as has been checked explicitly for $L = 3$ and $L = 6$. This is again in agreement with section 5.4. We note that the inclusion is strict (as expected by comparing the dimensions): the spin TM contains some eigenvalues which are not found in the RSOS representation.

We now compute the central charge from our finite- L free-energy estimates by using the standard CFT Ansatz

$$f_L(x) = f_{\text{bulk}}(x) + \frac{\pi G c(x)}{6L^2} + \frac{A(x)}{L^4}, \quad (47)$$

where $G = \sqrt{3}/2$ is the geometric factor for a triangular lattice on a torus. To exhibit the residual finite-size-scaling (FSS) corrections, we will fit the data to the Ansatz (47) for $L = L_{\min}, L_{\min} + 3, L_{\min} + 6$, and display the results as a function of L_{\min} . These results are shown in figure 11(b).

The results for the central charge are not unexpected: the critical points coincide with the solutions of the cubic (12) for $Q = 2$. There is a critical point in the ferromagnetic regime with $c_{\text{FM}} = 1/2$. We also find a zero-temperature critical point in the AF regime [4] with central charge $c = 1$ [5, 6]. Finally, we also find a $c_{\text{PF}} = 1/2$ critical point on the curve v_- , which lies in the unphysical region. Recall that this is expected, as there is numerical evidence [19] that $v_-(Q)$ for the triangular lattice belongs to the same universality class as

$v_{\text{AF}}(Q)$ for the square lattice [44, 45].[¶]

6.1.2. $Q = B_6 = 3$ The dimensions of the TM in the spin, FK, and RSOS representations are displayed in table 3, where again those of the RSOS case can be inferred from (41). In this case, we observe that there is an extra state in $\mathbb{T}_{\text{RSOS}}^{(\text{even})}$: $\dim \mathbb{T}_{\text{RSOS}}^{(\text{even})} - \dim \mathbb{T}_{\text{spin}} = 1$. The origin of this extra state can be found as follows: we split the RSOS variables in groups of two $g_i = h_{2i-1}h_{2i}$ for $1 \leq i \leq L$. Then in the *even* sector, each “word” g_i should start with 2 or 4, finish with 1, 3, 5, and respect the RSOS rule. Therefore there are 4 possible RSOS words, and we assign each of them to a spin value: $21 \rightarrow 1$, $23 \rightarrow 3$, $43 \rightarrow 3$, and $45 \rightarrow 1$. There is a one-to-one relation between RSOS and spin configurations, with a *single exception*: the spin configuration $11 \dots 1$ has two RSOS counterparts ($2121 \dots 21$) and ($4545 \dots 45$). Indeed, we need to assign $45 \rightarrow 1$ in order to be able to express e.g. spin configurations like $133 \rightarrow (454343)$.

We have computed the free energy (per site) for the different RSOS sectors defined in section 5, as well as the free energy in the spin representation, for each pair $(p, L) = (6, L)$ with $L = 3, 6, 9, 12, 15$. Also in this case, the quantities $f_L^{(\text{RSOS})}(p, x)$ and $f_L^{(\text{spin})}(Q, v)$ can only be guaranteed to agree for $x > 0$, since the RSOS model contains now three different boundary conditions, corresponding to giving the weight $Q_1 = 3$, $Q_2 = 1$ or $Q_3 = 0$ to each wrapping cluster. Only the first of those corresponds to periodic boundary conditions in the spin representation.

The absolute differences $\Delta_f(6, L)$, defined by (45), are listed in table 4. This is now non-zero for all symmetry sectors of the RSOS models. Notice that for $L = 12, 15$ we only have data for $f_L^{(\text{RSOS,even,F})}$, and in this case, only in the interesting ranges $x \in [-1.7, -0.4]$ and $x \in [-0.463, -0.456]$, respectively. In figure 12(a) we show the differences between $f_L^{(\text{spin})}$ and $f_L^{(\text{RSOS,even,F})}$ for $L = 3, 6, 9$.

We have also compared the full spectra of the RSOS and spin transfer matrices, finding the (sharp) inclusion

$$\text{sp } \mathbb{T}_L^{(\text{RSOS})}(x) \subset \bigcup_{a=1,2,3} \text{sp } \mathbb{T}_L^{(\text{spin}, a)}. \quad (48)$$

On the right-hand side, $a = 1$ corresponds to periodic boundary conditions on the spins. To get the $a = 2$ sector we must impose boundary conditions on the spins so that wrapping clusters in the corresponding FK model get the weight $Q_2 = 1$. We know that the spin is constant throughout a cluster, implying that its weight is equal to the number of possible spin labels that it can support. If we permute two of the spin labels when crossing the periodic direction, e.g., $(1, 2, 3) \rightarrow (2, 1, 3)$, a wrapping cluster can only support spins of the remaining third value, hence it will get the weight 1 indeed. We can therefore identify the $a = 2$ sector with \mathbb{Z}_2 -twisted boundary conditions. Similarly, if we permute all three

[¶] Our use of the subscripts FM and AF for the two $c = 1/2$ points does not imply that the two CFT are different in any way. But we shall soon see that the identification of c_{FM} and c_{PF} extends to other values of p as well.

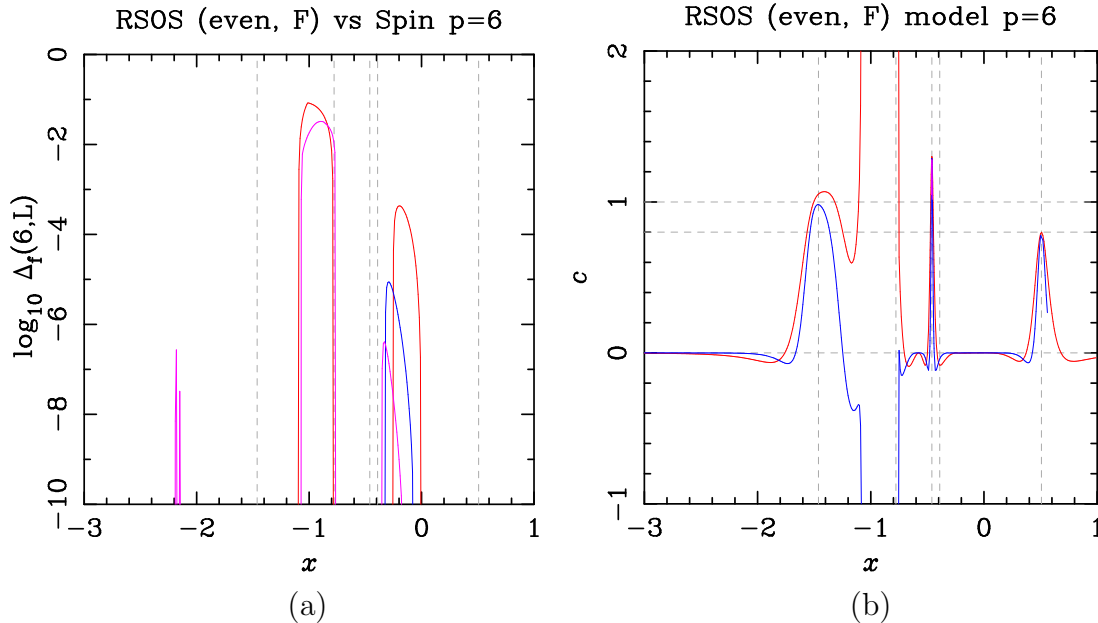


Figure 12. Free energy and central charge for the 3-state Potts model on a triangular lattice with toroidal boundary conditions and widths $L \equiv 0 \pmod{3}$ in the RSOS representation. (a) Absolute difference $\Delta_f(6, L)$ [cf. (45)] between $f_L^{(\text{spin})}$ and the free energy $f_L^{(\text{RSOS, even, F})}$ of the even sector of the RSOS model with all symmetries taken into account. We show the data for widths $L = 3$ (red), $L = 6$ (blue), and $L = 9$ (pink). (b) Central charge obtained from the Ansatz (47) and the RSOS data in the (even, F) sector. We display the results for $L_{\min} = 3$ (red), $L_{\min} = 6$ (blue), and $L_{\min} = 9$ (pink). The vertical dashed grey lines in both panels show the roots of Baxter’s cubic (12), the position of the first-order phase transition at $x = -0.46011(12)$ [28], and the position of the AF critical curve $x_{\text{AF}} \approx -0.39125$. The horizontal lines in (b) mark the expected results, $c_{\text{FM}} = 4/5$ and $c_{\text{PF}} = 1$.

spin labels cyclically, e.g., $(1, 2, 3) \rightarrow (2, 3, 1)$ across the seam, then wrapping clusters are disallowed altogether. Thus we can identify the $a = 3$ sector with \mathbb{Z}_3 -twisted boundary conditions. We have constructed the corresponding TM in the spin representation and verified (48) explicitly for sizes $L = 3$ and $L = 6$.

If we fit the RSOS free energy $f_L^{(\text{RSOS, even, F})}$ to the Ansatz (47) and use the same protocol as for $Q = 2$, we obtain the results displayed in figure 11(b). As expected, there is a peak at the ferromagnetic critical point with the central charge $c_{\text{FM}} = 4/5$ given by (43). At $x = -0.46010(2)$ we observe a sharp peak attaining the value $c = 1.265(15)$.⁺ This estimate for the central charge appears rather stable, but does not coincide with any known CFT possessing an S_3 symmetry. If this theory were conformal indeed, it might seem to challenge the works [28, 85], according to which the transition is (weakly) first order. But actually,

⁺ These central values and error bars are estimated from the following results for the position x_* and the value c_* of the peak in the three-point fit for the central charge: For $L = 3$, $x_* = -0.46019$ and $c_* = 1.3011$. For $L = 6$, $x_* = -0.46012$ and $c_* = 1.2886$. And for $L = 9$, $x_* = -0.46011$ and $c_* = 1.2796$.

having a discontinuity in the first derivative of the free energy (the hallmark of a first-order transition) is not incompatible with the transition being simultaneously second-order (and conformal): indeed, this scenario was found for the AF transition in the square-lattice Potts model [19]. In any case, determining the exact nature of this transition would require further work; Density-matrix-renormalisation-group (DMRG) simulations for larger sizes would be one option.

In the (unphysical) region in between the central and lower branches of the cubic (12), we find large absolute values of the central charge, which are not expected to be physical at all. As a matter of fact, the fits of the spin free energy $f_L^{(\text{spin})}$ to the Ansatz (47) for $L = 3, 6, 9$ give very similar results to those depicted in figure 12(b) for $L_{\min} = 3$, even in that region. These observations may imply that none of these models are well defined in this interval, or that we need data for larger widths in order to obtain meaningful physical results there.

Finally, at the lower branch $x_- = v_-/\sqrt{3} \approx -1.4619$, we find a peak with a central charge $c = 0.98(2)$. This is compatible with the expected result $c_{\text{PF}} = 1$.

6.2. Results for non-integer values of Q

In this section we will discuss the cases $p = 5, 7, 8$. As Q is not an integer, we do not have immediate access to the spin representation (but see also [86]). We can however still compare our results with those of the FK representation. Notice that for any of the three values of p , we do not find any vanishing amplitude and/or eigenvalue cancellation for the FK model, at least not for $L = 3$, and so the non-local aspects of FK clusters would seem to remain present in the corresponding partition function on the torus. Therefore, it is not clear to us to which extent the FK and RSOS models can be considered equivalent for such values of p . In any case, we shall henceforth pursue the study of the RSOS model in its own right.

In table 5 we show the dimensions of the TM in the FK representation and in the RSOS representation in the even sector, and in the same sector with all symmetries taken into account. Notice that when p is odd, then the symmetry $h \rightarrow p - h$ mixes both sectors, so in this case we only consider the rotational symmetry. On the contrary, when p is even, we consider all (i.e., spin reversal and rotational) symmetries. The dimensions of $\mathbb{T}_{\text{RSOS}}^{(\text{even})}$ and $\mathbb{T}_{\text{RSOS}}^{(\text{odd})}$ agree of course with (41).

6.2.1. $Q = B_5$. In this case we find that the free energies satisfy $f_L^{(\text{RSOS,even,F})} = f_L^{(\text{RSOS,odd,F})}$, so we will consider the former in our analysis. If we compare $f_L^{(\text{RSOS,even,F})}$ with the free energy of the Potts model with $Q = B_5$ in the FK representation $f_L^{(\text{FK})}$, we see in figure 13(a) that they disagree strongly in an interval that starts close to the lower branch of the cubic v_- (12) and finish at the position of the AF critical curve $v_{\text{AF}} \approx -0.35065$. In the remainder of the interval $x \in [-3, 1]$, the agreement between these two free energies is perfect (within the numerical precision). Indeed, for $x \geq 0$ this is expected, since then the FK representation has a probabilistic interpretation, and we can argue (like in [82]) that

p	L	$\dim \mathbb{T}_{\text{FK}}$	$\dim \mathbb{T}_{\text{RSOS}}^{(\text{even})}$	$\dim \mathbb{T}_{\text{RSOS}}^{(\text{even}, \text{F})}$
5	3	30	18	8
	6		322	60
	9		5778	648
	12		103682	
7	3	30	38	16
	6		1186	210
	9		40169	4475
	12		1373466	
8	3	30	48	10
	6		1648	148
	9		63552	3538
	12		2513024	

Table 5. Dimension of the TM for the Potts model with $Q = B_p$ ($p = 5, 7, 8$) on a triangular-lattice strip graph on the torus in the FK representation \mathbb{T}_{FK} , and in the RSOS representation in the *even* sector $\mathbb{T}_{\text{RSOS}}^{(\text{even})}$, and in the same sector with all symmetries $\mathbb{T}_{\text{RSOS}}^{(\text{even}, \text{F})}$. Note that $\dim \mathbb{T}_{\text{RSOS}}^{(\text{even})} = \dim \mathbb{T}_{\text{RSOS}}^{(\text{odd})}$.

these two models should be equivalent in the ferromagnetic regime.

We have fitted the free-energy data $f_L^{(\text{RSOS}, \text{even}, \text{F})}$ to the CFT Ansatz (47) and used the same protocol as for the other cases. The results are displayed in figure 13(b). As expected, we find a peak at the ferromagnetic critical point with the central charge $c_{\text{FM}} = 7/10$. A closer look at this figure reveals four other interesting regions:

- (i) A broad peak close to $x_- = v_-/\sqrt{B_5} \approx -1.6180$ with central charge $c = 0.797(3)$. This is in perfect agreement with the expected result $c_{\text{PF}} = 4/5$. [See figure 14(a)].
- (ii) A broad plateau in the interval $x \in (x_-, -1.14]$ with a constant central charge $c = 0.70(1)$. [See figure 14(a)].
- (iii) A narrow plateau in the interval $x \in [-0.61, -0.57]$ with a constant central charge $c = 0.800(2)$. [See figure 14(b)].
- (iv) A narrow peak at $x = -0.4883(1)$ with central charge $c = 1.198(2)$. [See figure 14(b)].[†]

We conjecture that the exact values of the central charge on the two plateaux, (ii) and (iii), are $c = 7/10$ and $c = 4/5$ respectively. Note that these values coincide with c_{FM} and c_{PF} , respectively, and hence we can presumably identify them with the corresponding

[†] These central values and error bars are estimated from the following results for the position x_* and the value c_* of the peak in the three-point fit for the central charge: For $L = 3$, $x_* = -0.48833$ and $c_* = 1.2069$. For $L = 6$, $x_* = -0.48828$ and $c_* = 1.2038$. And for $L = 9$, $x_* = -0.48829$ and $c_* = 1.2016$.

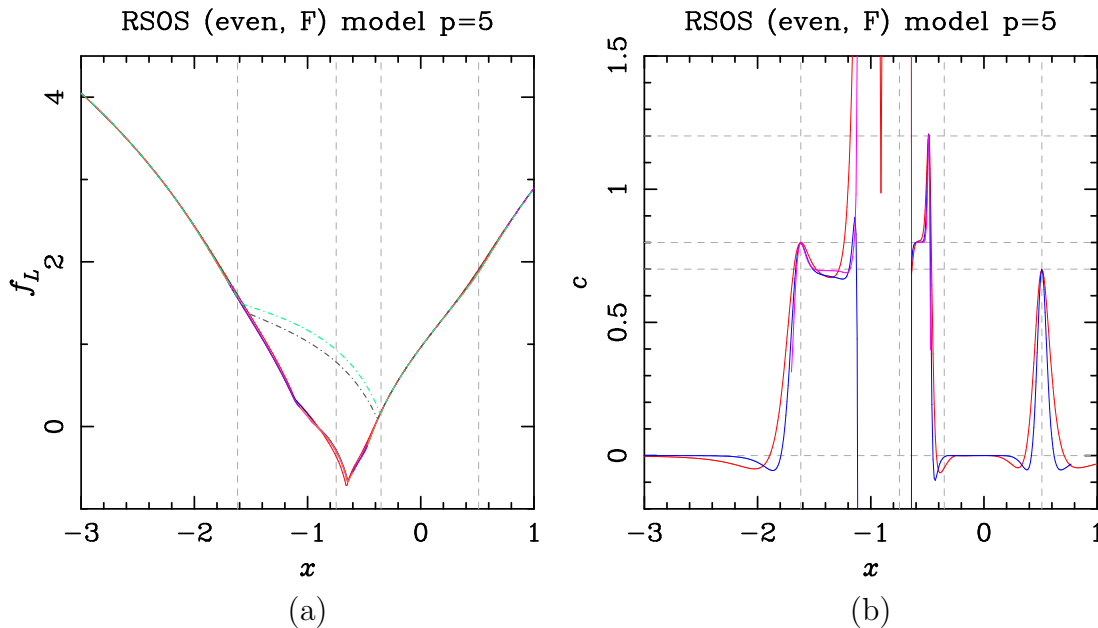


Figure 13. Free energy and central charge for the RSOS model with $p = 5$ on a triangular lattice with toroidal boundary conditions and widths $L \equiv 0 \pmod{3}$. (a) The solid curves depict the free energy $f_L^{(\text{RSOS,even,F})}$ of the even sector of the RSOS model with all symmetries taken into account. We show the data for widths $L = 3$ (red), $L = 6$ (blue), $L = 9$ (pink), $L = 12$ (orange), and $L = 15$ (violet). The dot-dashed curves show the free energy in the FK representation $f_L^{(\text{FK})}$ for widths $L = 3$ (violet), and $L = 6$ (dark grey). (b) Central charge obtained from the Ansatz (47) and the RSOS data in the (even, F) sector. We display the results for $L_{\min} = 3$ (red), $L_{\min} = 6$ (blue), and $L_{\min} = 9$ (pink). The vertical dashed grey lines in both panels show the roots of Baxter's cubic (12), and the position of the AF critical curve $x_{\text{AF}} \approx -0.35065$. The horizontal lines in (b) mark the expected results $c_{\text{FM}} = 7/10$ and $c_{\text{PF}} = 4/5$, as well as our conjectured new value, $c = 6/5$.

CFT. Each plateau appears to be controlled by an attractive fixed point of the indicated nature, at it would be interesting to examine further why the temperature variable x does not couple to any of the relevant operators present in those fixed-point theories. It would also be interesting to study further the precise nature of the flow from the $c = 1.198(2)$ theory (iv) towards the $c = 4/5$ plateau (iii), and the flow from the $c_{\text{PF}} = 4/5$ theory (i) towards the $c = 7/10$ plateau (ii).

We further conjecture that the exact value of the central charge at the peak (iv) is $c = 6/5$. Perhaps we can split this result as $6/5 = 1/2 + 7/10$, so that this model corresponds to a model belonging to the same universality class as the ferromagnetic one plus an Ising fermion. The flow from the peak (iv) towards the fixed point controlling the plateau (iii) could then be characterised by this fermion becoming massive.

Notice that the result $c_{\text{PF}} = 4/5$ at the peak (i) can also be produced by evaluating c_{FM} with $p \rightarrow p + 1$. Therefore we can speculate that the flow from (i) to (ii) is just the usual flow between minimal models, $\mathcal{M}_p \rightarrow \mathcal{M}_{p-1}$.

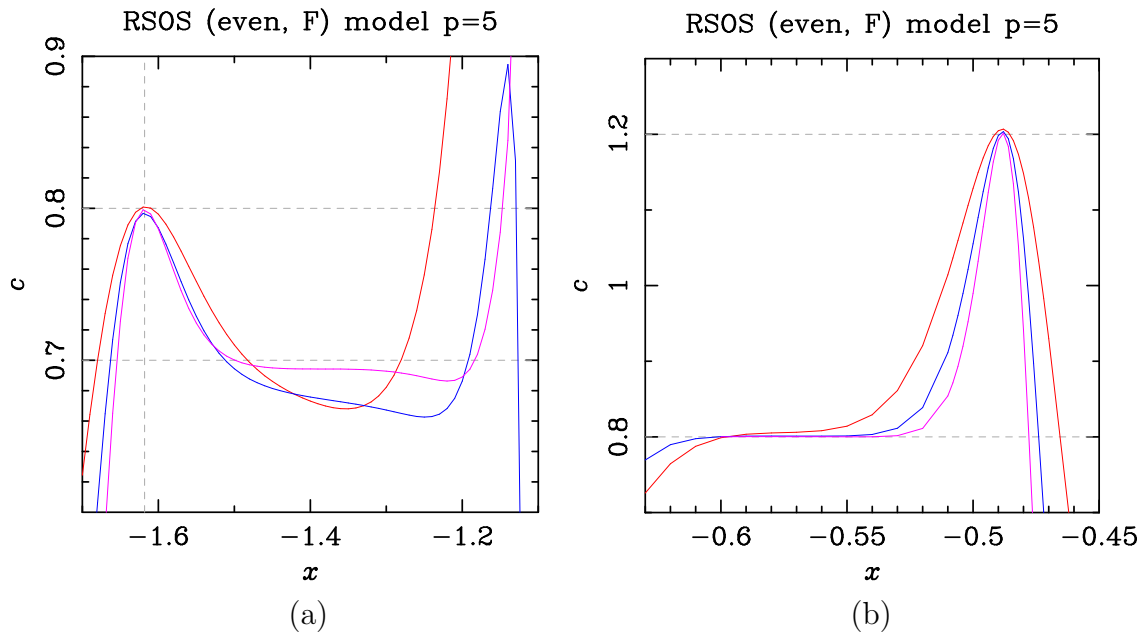


Figure 14. Zooms of figure 13(b) close to the two most interesting regions: $x \in [-1.7, -1.1]$ (a) and $x \in [-0.5, -0.45]$ (b). In each panel, we show the central charge obtained from the Ansatz (47) with $L_{\min} = 3$ (red), $L_{\min} = 6$ (blue), and $L_{\min} = 9$ (pink). Vertical and horizontal dashed grey lines have the same meaning as in figure 13.

Finally, it should be remarked that the zero-temperature point in the AF regime corresponds to $x = -1/\sqrt{B_5} \approx -0.6180$, which is very close to the lower bound of the interval defining the plateau (ii). It is possible that this value is indeed the termination point of the plateau. In addition, the region containing the interval $x \in [-1.1, -0.8]$ shows estimates for the central charge that are rather large in absolute value, and hence presumably unphysical or at least non-critical, similar to the behavior we found for $p = 6$ in approximately the same region.

6.2.2. $Q = B_7$ The situation is very similar to the $p = 5$ case. Again we find that $f_L^{(\text{RSOS,even,F})} = f_L^{(\text{RSOS,odd,F})}$. If we compare any of them with the free energy of the Potts model with $Q = B_7$ in the FK representation $f_L^{(\text{FK})}$, we see in figure 15(a) that they disagree in the interval $x \in [x_-, x_{\text{AF}}]$, where $x_- = v_- \sqrt{B_7} \approx -1.3686$, and $x_{\text{AF}} \approx -0.41812$.

We have fitted the free-energy data $f_L^{(\text{RSOS,even,F})}$ to the CFT Ansatz (47); the results are displayed in figure 15(b). In addition to the expected peak at the ferromagnetic critical point with the usual central charge $c_{\text{FM}} = 6/7 \approx 0.8571$, we find a similar structure to that of the $p = 5$ case:

- (i) A broad peak close to $x_- = v_-/\sqrt{B_7}$ with central charge $c = 1.12(1)$. This agrees with the general result $c_{\text{PF}} = 8/7 \approx 1.1429$.
- (ii) Just to the right of that peak, it is possible that a plateau is nascent in the $L = 12$ data, but it would clearly require larger system sizes to confirm the reality of this feature.

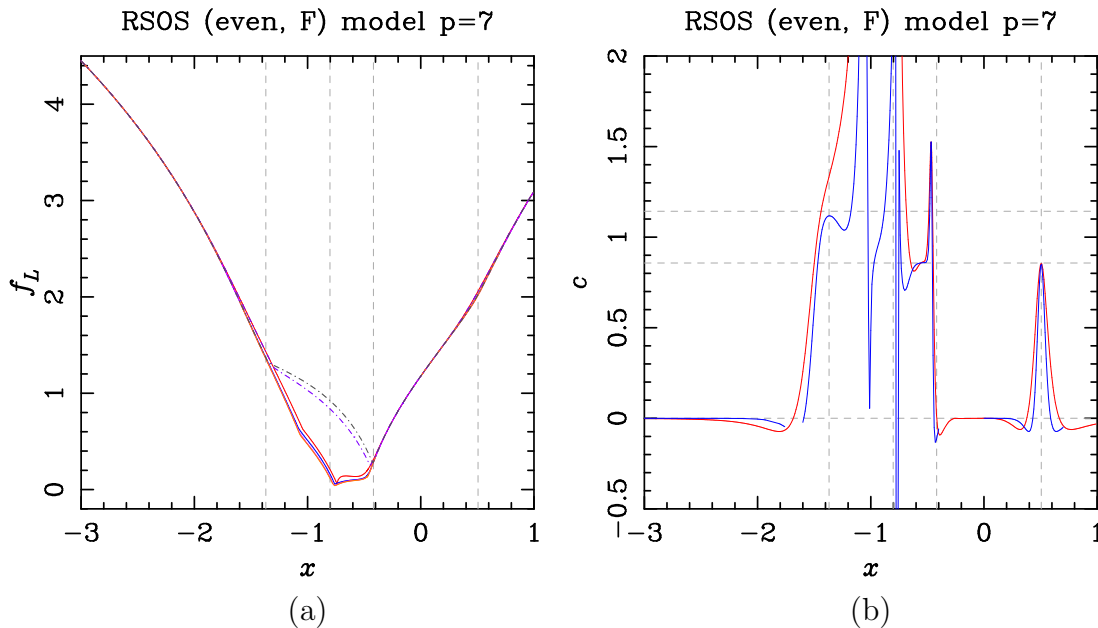


Figure 15. Free energy and central charge for the RSOS model with $p = 7$ on a triangular lattice with toroidal boundary conditions and widths $L \equiv 0 \pmod{3}$. (a) The solid curves depict the free energy $f_L^{(\text{RSOS,even,F})}$ of the even sector of the RSOS model with all symmetries taken into account. We show the data for widths $L = 3$ (red), $L = 6$ (blue), $L = 9$ (pink), and $L = 12$ (orange). The dot-dashed curves show the free energy in the FK representation $f_L^{(\text{FK})}$ for widths $L = 3$ (violet), and $L = 6$ (dark grey). (b) Central charge obtained from the Ansatz (47) and the RSOS data in the (even, F) sector. We display the results for $L_{\min} = 3$ (red) and $L_{\min} = 6$ (blue). The vertical dashed grey lines in both panels show the roots of Baxter's cubic (12), and the position of the AF critical curve $x_{\text{AF}} \approx -0.41812$. The horizontal lines in (b) mark the expected results, $c_{\text{FM}} = 6/7$ and $c_{\text{PF}} = 8/7$.

- (iii) A very narrow plateau in the interval $x \in [-0.58, -0.51]$ with an approximately constant central charge $c = 0.859(2)$. This value is compatible with $c_{\text{FM}} = 6/7 \approx 0.8571$. [See figure 16(a)].
- (iv) A narrow peak at $x = -0.4669(2)$ with central charge $c \approx 1.53$. Given the scarcity of available sizes, it does not appear reasonable to give any error bar on this result, or even claim convergence to a finite value. In any case, there is no obvious candidate CFT with this value of the central charge. Notice that this peak is below our estimate for the AF critical curve $x_{\text{AF}} \approx -0.41812$. (See figure 15).

The lower bound of the AF regime $x = -1/\sqrt{B_7} \approx -0.5550$ is again rather close to the lower end of the plateau (ii).

6.2.3. $Q = B_8$ Again, the situation is very similar to the previous two cases ($p = 5$ and $p = 7$). We find that $f_L^{(\text{RSOS,even,F})} = f_L^{(\text{RSOS,odd,F})}$, and if we compare any of them with the free energy of the Potts model with $Q = B_8$ in the FK representation $f_L^{(\text{FK})}$, we see in figure 17(a)

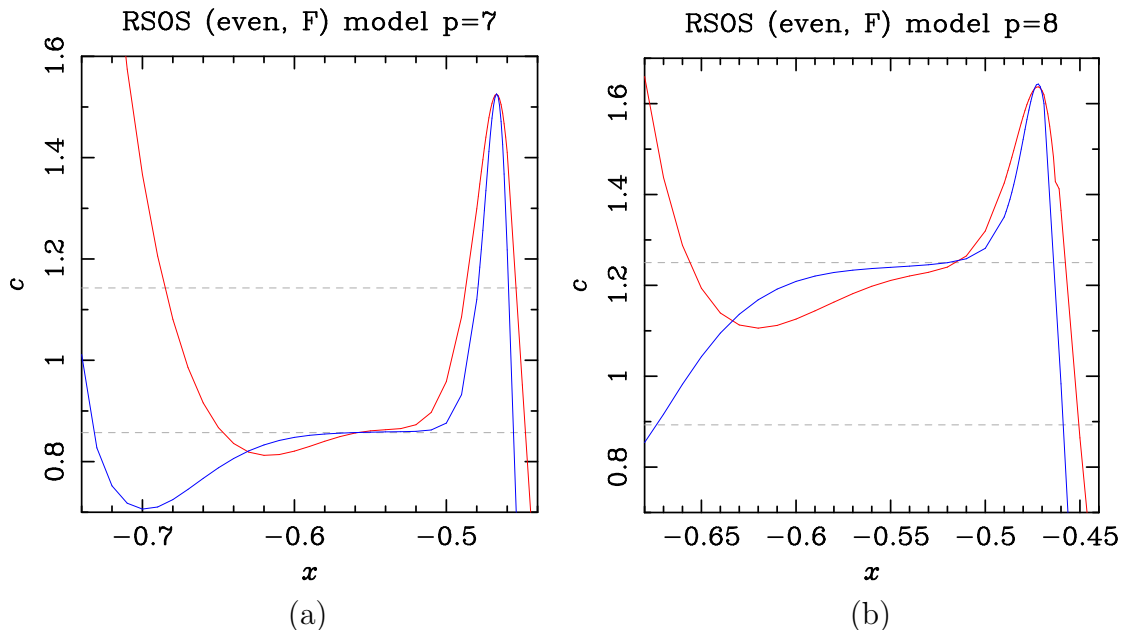


Figure 16. Zooms of figure 15(b) in the interval $x \in [-0.74, -0.44]$ (a), and of figure 17(b) in the interval $x \in [-0.68, -0.44]$ (b). In each panel, we show the central charge obtained from the Ansatz (47) with $L_{\min} = 3$ (red), $L_{\min} = 6$ (blue), and $L_{\min} = 9$ (pink). Vertical and horizontal dashed grey lines have the same meaning as in figure 13.

that they strongly disagree in the interval $x \in [x_-, x_{\text{AF}}]$, where $x_- = v_- \sqrt{B_8} \approx -1.3066$, and $x_{\text{AF}} \approx -0.43783$ is our estimate for the position of the AF critical curve. There is another interval where we found differences, $x \in [-0.33, -0.05]$, but in this case the differences decrease as L increases.

We have fitted the free-energy data $f_L^{(\text{RSOS,even,F})}$ to the CFT Ansatz (47); the results are displayed in figure 17(b). In this case, the results are less clear than for $p = 5, 7$; the FSS corrections seem to be stronger, so we would need larger sizes to draw more definitive conclusions. Indeed, we find a ferromagnetic peak with the expected central charge $c = 25/28 \approx 0.8929$. Although there is no trace of the peak at the lower branch of the cubic $x_- \approx -1.3066$, the curve for the largest system sizes convincingly passes through the right value, $c_{\text{PF}} = 5/4$. The plateau starting close to the zero-temperature AF point $x \approx -0.5412$ is at best emergent, in the form of a shoulder. The clearest feature that remains is a sharp peak at $x = -0.4722(1)$, with central charge $c \approx 1.64$. Like in the $p = 7$ case, larger sizes would be necessary to corroborate this result. As for the other values of p , this peak is below the AF critical curve $x_{\text{AF}} \approx -0.43783$ (see figure 17).

7. Physical conclusions

The first goal of this paper was to compute the AF critical curve for the triangular-lattice Q -state Potts model. This was not, by any means, a simple computation because of the

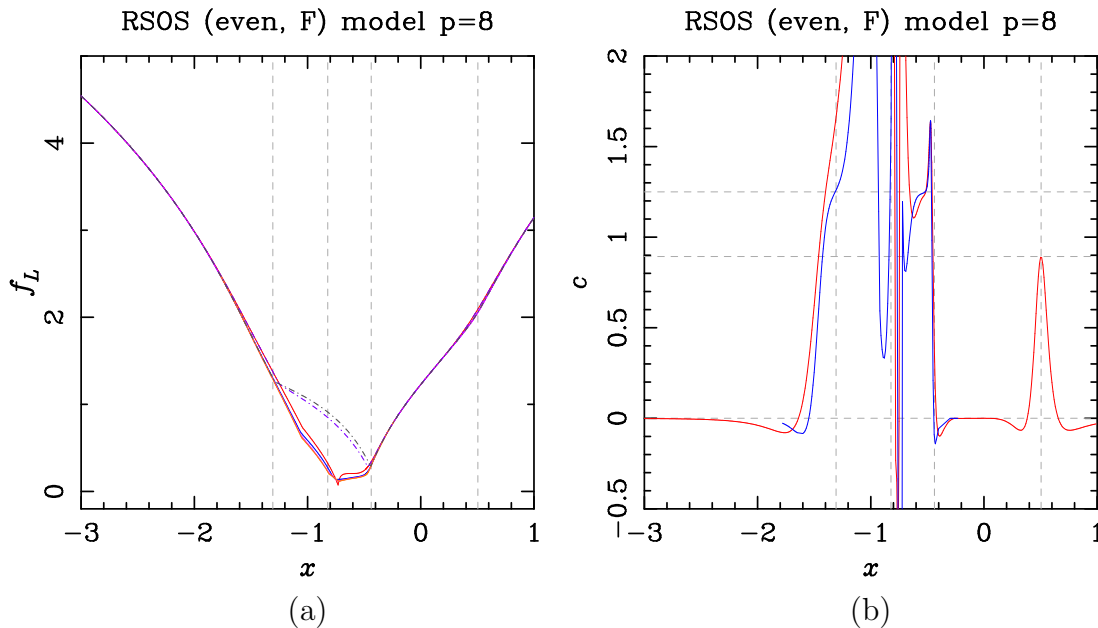


Figure 17. Free energy and central charge for the RSOS model with $p = 8$ on a triangular lattice with toroidal boundary conditions and widths $L \equiv 0 \pmod{3}$. (a) The solid curves depict the free energy $f_L^{(\text{RSOS,even,F})}$ of the even sector of the RSOS model with all symmetries taken into account. We show the data for widths $L = 3$ (red), $L = 6$ (blue), $L = 9$ (pink), and $L = 12$ (orange). The dot-dashed curves show the free energy in the FK representation $f_L^{(\text{FK})}$ for widths $L = 3$ (violet), and $L = 6$ (dark grey). (b) Central charge obtained from the Ansatz (47) and the RSOS data in the (even, F) sector. We display the results for $L_{\min} = 3$ (red) and $L_{\min} = 6$ (blue). The vertical dashed grey lines in both panels show the roots of Baxter’s cubic (12), and the position of the AF critical curve $x_{\text{AF}} \approx -0.43783$. The horizontal lines in (b) mark the expected results, $c_{\text{FM}} = 25/28$ and $c_{\text{PF}} = 5/4$.

existence of a T-point. We have used two complementary methods: limiting curves obtained from the TM approach, and the graph polynomial method.

The TM method required to build the TM for triangular-lattice strip graphs with toroidal boundary conditions in the FK representation. We chose these boundary conditions as they are expected to give results closer to the thermodynamic limit (as shown in [53] for the chromatic polynomial); but they require to work with larger connectivity spaces and the use of many technicalities [53]. These two factors severely limit the maximum strip width one can deal with symbolically, but nevertheless, one can increase this width by performing the computation numerically. With this technique we were able to obtain an accurate approximation to the AF critical curve for $0 \leq Q \lesssim 3.6$. The T-point $T = (Q_T, v_T)$ [cf. (32)] is rather close to the upper limit of such interval, so we expect large FSS corrections to take place, as well as parity effects mod 3 for the interval $Q \in [3.6, 4]$.

On the other hand, the graph polynomial method provides also very accurate estimates for the AF critical curve, specially for the interval $Q \in [0, 2]$; but it missed some regions, like

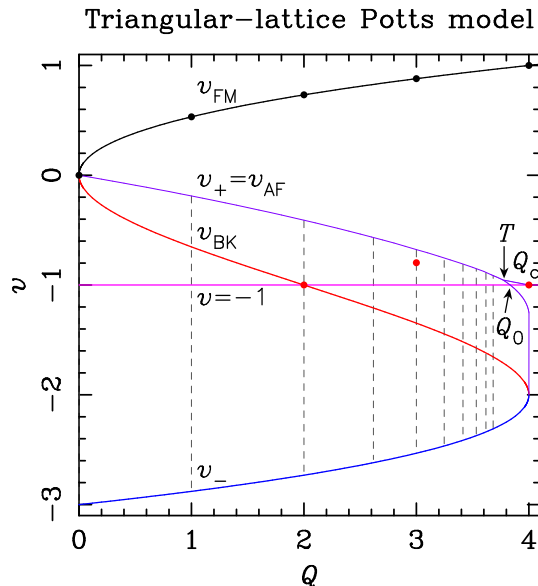


Figure 18. Phase diagram of the triangular-lattice Q -state Potts model in the real (Q, v) plane. (Compare to figure 1.) The cubic (12) corresponds to the three thick lines labeled v_{FM} , v_{BK} , and v_- , respectively. The horizontal line corresponds to $v = -1$ (13). The curve between v_{FM} and v_{BK} is our best numerical estimate of the AF curve $v_+ = v_{\text{AF}}$ for this lattice. This curve has a bifurcation point T, leading to two branches: one goes to the point $(Q_0, -1)$ [cf. (16)], while the other goes to the critical point $(4, -1)$. The region defined by these three points and $(4, v_1)$ [cf. (31)] is governed by regime IV, while the BK phase corresponds to regime I. The vertical dashed lines correspond to the Beraha numbers B_p [cf. (7)], shown here for $3 \leq k \leq 11$. The solid dots depict the known critical points for integer values of Q .

the curve in the interval $Q \in (2, 3)$, and the branch going from the T point down to $(4, v_1)$ [cf (31)]. By combining the data obtained from these two methods, we were able to have a rather accurate estimate for the position of the AF critical curve in the (Q, v) -plane. This curve is shown in figure 18. The phase diagram of the triangular-lattice Q -state Potts model is now complete at least for $Q \in [0, 4]$.

It is worth noticing that now we have a consistent renormalisation-group (RG) flow at least for $Q \in [0, 4]$, which is rather similar to (but richer than) the RG flow for the same model on the square lattice. For a given value of Q (which is not changed by the RG flow), we find that the temperature is a relevant operator on the ferromagnetic and AF critical curves (v_{FM} and v_{AF} , respectively), and on the lower branch of the cubic curve v_- . For v_{FM} , the RG flow is towards the trivial zero-temperature $v \rightarrow \infty$ and infinite-temperature $v = 0$ fixed points. For v_- the RG flow is towards the BK phase and the trivial unphysical $v \rightarrow \infty$ fixed points.

Inside the BK phase, there is a non-trivial fixed point, which can be identified with the curve v_{BK} . Note that the integrable chromatic line $v = -1$ is also in the BK universality class [20] inside Regime 1, i.e., for $0 \leq Q \leq Q_0$, with Q_0 given by (16). However, since only

the middle branch v_{BK} of the cubic (12) exists for all $Q \in [0, 4]$, it must be the latter that acts as the RG attractor inside the BK phase.

Finally, above the AF critical curve, the RG flow is towards the trivial infinite-temperature $v = 0$ fixed point. Below that curve, for $0 \leq Q < Q_0$ it flows to the BK phase fixed point v_{BK} , and for $Q_0 < Q \leq 4$ it flows to the chromatic polynomial fixed point $v = -1$ governed by the so-called Regime IV [20]. Let us recall that in both phases (BK and Regime IV) the temperature is an irrelevant operator.

Although the phase diagram for the triangular-lattice Q -state Potts model is thus well understood for $Q \in [0, 4]$, we find that for $Q > 4$ there are additional features whose full comprehension would require more work. In the TM approach, we find “phases” characterised by a pair of complex conjugate dominant eigenvalues (instead of the more common situation in which there is a single dominant eigenvalue). These phase are denoted by ℓ^* (with $0 \leq \ell \leq 3$) in figure 5. These phases even appear close to the curve v_- for $0 \leq Q \leq 1$, although their extension seems to shrink as the strip width increases. This means that partition-function zeros will accumulate not only along the usual limiting curves, but also throughout these regions. This unusual feature previously appeared when studying the phase diagram in the (Q, v) -plane of the Q -state Potts model on the generalised Petersen graphs [67]. In the critical-polynomial approach, we also find new structures for $Q > 4$ [see figure 8(a)]. In both approaches, the phase-diagram features for $Q > 4$ look like a band extending towards large Q (perhaps even to $Q \rightarrow \infty$); but the FSS corrections are rather large and prevent us from drawing any definitive conclusion [see figures 6(a) and 8(a).]

The features of the phase diagram of the triangular-lattice Q -state Potts model described this far are expected to be independent of the boundary conditions used in the computations (once all the FSS effects are removed). Therefore, we can use the above conclusions to deduce the phase diagram of the hexagonal-lattice model as well. Even though duality for the Potts model only applies to planar graphs [13], we can nevertheless apply it to the phase diagram in the thermodynamic limit. Therefore, any curve $v(Q)$ in the triangular-lattice phase diagram will transform into its dual curve $v^*(Q) = Q/v(Q)$ in the hexagonal-lattice phase diagram. In this way we deduce the phase diagram of the hexagonal-lattice Q -state Potts model (depicted in figure 19) from figure 18. Indeed, the RG flows are similar to those for the triangular-lattice discussed above.

Notice that duality relates v_{FM} and v_{BK} in both models. More precisely, under duality $v_{\text{F,tri}} \leftrightarrow v_{\text{F,hex}}$ and $v_{\text{BK,tri}} \leftrightarrow v_{\text{BK,hex}}$. Therefore, we expect the same critical behavior on both lattices for both the ferromagnetic critical curve v_{FM} and the BK phase. Indeed, there is no surprise in these observations.

On the other hand, duality interchanges the role played by v_{AF} and v_- : i.e., $v_{\text{AF,tri}} \leftrightarrow v_{-,hex}$ and $v_{-,tri} \leftrightarrow v_{\text{AF,hex}}$. In [19] it was numerically shown that $v_{-,tri}(Q)$ belongs to the same universality class as the AF critical curve for the square-lattice model [44, 45] for the same value of Q . Notice that for the hexagonal lattice $Q_c = B_5$, while for the square lattice, $Q_c = 3$. Therefore, we conjecture that the AF critical curves $v_{\text{AF}}(Q)$ for the hexagonal-

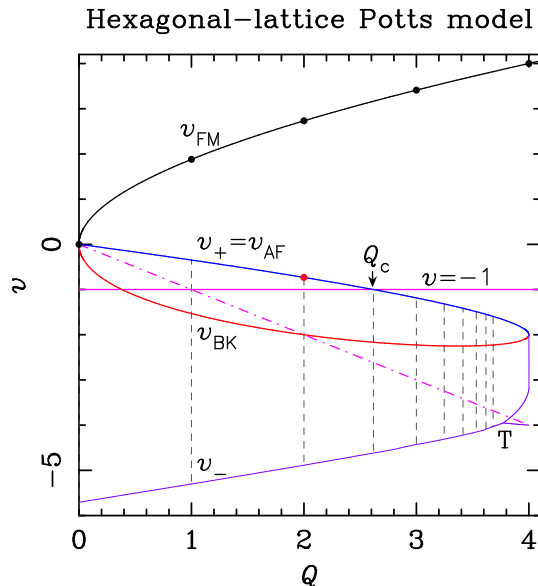


Figure 19. Phase diagram of the hexagonal-lattice Q -state Potts model in the real (Q, v) plane. The lines use the same colour code as in figure 18 to make the comparison easier. The cubic (12) now corresponds the “dual cubic” $v^3 - 3Qv = Q^2$. Its three branches are v_{FM} , v_{AF} , and v_{BK} . The dual of the AF critical curve of the triangular-lattice model now plays the role of v_- . The horizontal (pink) line corresponds to $v = -1$, and $Q_c(\text{hex}) = B_5$. The inclined dot-dashed (pink) line corresponds to $v = -Q$ for $0 \leq Q \leq 4$, where the model is integrable. The vertical dashed lines correspond to the Beraha numbers B_p [cf. (7)], shown here for $3 \leq p \leq 11$. The solid dots depict the known critical points for integer values of Q .

and square-lattice Q -state Potts models belong to the same universality class at least for $Q \in [0, B_5]$.

The second main goal of this paper is to study the triangular-lattice RSOS model on the torus. Indeed, when $Q = B_p$ [cf. (7)] for integer $q \geq 3$, and we are in a probabilistic regime (i.e., $v \geq 0$ or $x \geq 0$), then the Q -state Potts model and the corresponding RSOS model of type A_{p-1} give the same free energy [82]. But in the AF or the unphysical regimes, this property does not have to hold in general. In particular, this fact opens the possibility of finding distinct critical phenomena; as it already happened when the RSOS model was studied on the square lattice [19]. Moreover, in these latter regimes, universality is not expected to hold, so it seems very interesting to consider the triangular-lattice RSOS model on the torus, and see whether there are new features and/or they are universal or model-dependent.

In this paper, we have built the TM for the triangular-lattice RSOS model on the torus for $4 \leq p \leq 8$, and strip widths $L = 3, 6, 9, 12, 15$ (to avoid mod 3 parity effects). Unfortunately, as p increases, the number of states also increases exponentially fast, so for $p = 7, 8$ we could only compute data up to $L = 12$. This means in practice that the features of the RSOS model (e.g., its central charge as a function of x) become less amenable to

numerical investigations as p increases. The behavior of this model (compared to that of the Q -state Potts model in the FK and/or spin representation) is somewhat different depending on whether Q is an integer or not.

When Q is an integer (i.e., $p = 3, 4, 6$), we have compared the RSOS results to those coming from TM in both the FK and spin representations. In the former case, we have explicitly checked for $L = 3$ that there are eigenvalue cancellations, and vanishing amplitudes, as it happens for other strip graph families when $Q = B_p$ [52, 53, 67]. But we have used the results obtained from the TM in the spin representation (for widths up to $L = 12$) as a comparison for the RSOS results. The first non-trivial value corresponds to $p = 4$ ($Q = 2$). Even though we obtained a phase diagram with no surprises at all, it is remarkable that we have numerically observed that the full spectrum of the RSOS model on the torus is strictly contained in the union of the spectra of the corresponding Ising models on the torus with periodic and anti-periodic boundary conditions, respectively, in accord with recent results on braid translation in the blob algebra [84]. This feature is also present for $p = 6$ ($Q = 3$), but in this case, the sum is over three boundary conditions we can impose for the spin model on the torus: i.e., periodic, \mathbb{Z}_2 - and \mathbb{Z}_3 -twisted boundary conditions.

Still for $p = 6$, in addition to the expected peaks in the central charge located at x_{FM} and x_- , we find two interesting features that merit some comments. First, there is a region approximately in the interval $x \in [-1.07, -0.77]$ where the absolute value of the central charge takes large values that cannot be considered physical. This region is contained in the BK phase, and it is an open question to know what is the real behavior of the RSOS model in that interval. Secondly, we find a sharp peak at $x = -0.46010(2)$, which coincides within errors with the position $x = -0.460106(12)$ of the (weak) first-order phase transition found in [85]. The value of the central charge at this peak is rather stable $c = 1.265(15)$. The interpretation of this numerical result is not clear, and we leave it as an open problem for future considerations.

When Q is a non-integer (i.e., $p = 5, 7, 8$), we can only compare our results with those coming from the TM in the FK representation. In particular, we find that for $L = 3$ in the FK representation, there are no eigenvalue cancellations and/or vanishing amplitudes when $Q = B_p$. This feature can be explained if we take into account that the toroidal triangular-lattice strip graphs are not planar. In this case, we should expect these cancellations to occur only at positive integers, as conjectured in [67]. By simple inspection of figures 13(a), 15(a), and 17(a), it is clear that the free energies for the RSOS and Potts models differ in the whole BK phase: i.e. in the interval $x \in [x_-, x_{\text{AF}}]$. Outside this interval (including of course the probabilistic regime $x \geq 0$), the ground states of those two models have the same free energy. Notice that (as in the $p = 6$ case) there is a region around $x = -1$ where the central charge becomes unexpectedly large in absolute value. Again, we need further studies with larger widths to disentangle the physics in this region.

Even though our results are less clear as p is increased, there are clear indications (at least for $p = 5, 7$) that there are regions with *new* physics. Let us review these findings in

some detail:

- For $p = 5$ it is clear that, in addition to the expected central charge peak at $x = x_-$ with value given by c_{PF} , there is a plateau for $x \in [x_-, -1.14]$, where the central charge stays approximately constant: i.e., $c = 0.70(1)$, which agrees within errors with $c_{\text{FM}} = 7/10$. For $p = 7$, the peak at x_- can be seen, but we need data with larger values of L to see whether there is a similar plateau to the right of the peak.
- For $p = 5, 7, 8$ there is a sharp peak just below the AF critical curve v_{AF} . Its position and the central charge attained at its maximum is $x = -0.4833(1)$ and $c = 1.198(2)$ for $p = 5$; $x = -0.4669(2)$ and $c \approx 1.53$ for $p = 7$; and $x = -0.4722(1)$ and $c \approx 1.64$ for $p = 8$. As p increases, the position of the maximum becomes more negative, and at the same time, it becomes closer to v_{AF} . In addition, the value of the central charge increases as p increases. It is worth mentioning that the peak found for the first-order phase transition at $p = 6$ ($x = -0.46010(2)$ and $c = 1.265(15)$) fits perfectly in this general behavior. This seems to be a general feature of the model, but additional work is needed in order to investigate the nature of these peaks: i.e., whether there is a first-order phase transition, or a critical point, or a transition that is first- and second-order at the same time (like the AF critical curve for the square-lattice Q -state Potts model [19]). If (some of) the transitions are second order, then one would need to identify the corresponding CFT.
- For $p = 5, 7, 8$ there are clear indications of the existence of a narrow plateau close and to the left of the previous peak with values that seem to alternatively agree with either c_{PF} or c_{FM} . In particular, for $p = 5$ the plateau corresponds to the interval $x \in [-0.61, -0.57]$ with central charge $c = 0.800(2)$, which agrees within errors with $c_{\text{PF}} = 4/5$. For $p = 7$ the plateau is given by the interval $x \in [-0.58, -0.51]$ with central charge $c = 0.859(2)$, which is compatible with $c_{\text{FM}} = 6/7$. Finally, for $p = 8$ we one find some hints of a nascent plateau around $x \approx -1.54$ with $c \approx c_{\text{PF}} = 5/4$. We need more data to give a more precise account of this feature.

The understanding of these new critical regions, and the RG flow among them remain as interesting open problems, which are outside the scope of this paper.

Appendix A. Amplitudes for the triangular-lattice Potts model

In this appendix we will display which amplitudes α_k appear in the partition function for the Q -state Potts model on a triangular-lattice strip graph of width L and periodic boundary conditions in the FK representation (24). Let us start with the particular case $v = -1$ [53], and then we will move on to the general case.

Appendix A.1. Chromatic polynomial

Chang and Shrock [87] found a family of basic amplitudes $\beta^{(\ell)}$ for $\ell \geq 0$ that could be written in terms of the amplitudes $\alpha^{(\ell)}$ for strip graphs with cyclic boundary conditions [88]:

$$\beta^{(\ell)} = \begin{cases} \alpha^{(\ell)} & \text{for } \ell = 0, 1, \\ \alpha^{(\ell)} - \alpha^{(\ell-1)} + (-1)^\ell \alpha^{(1)} & \text{for } \ell \geq 2. \end{cases} \quad (\text{A.1})$$

The amplitudes $\alpha^{(\ell)}$ are expressed in terms of the Chebyshev polynomial of second kind U_n :

$$\alpha^{(\ell)}(Q) = U_{2\ell} \left(\frac{\sqrt{Q}}{2} \right). \quad (\text{A.2})$$

In this paper we need the amplitudes $\beta^{(\ell)}$ for $0 \leq \ell \leq 6$ [52, equation (2.31)].

Moreover, Chang and Shrock noted that for $\ell \geq 2$, these amplitudes split in several parts. Richard and Jacobsen proved this fact, and gave an explicit expression for the relevant amplitudes $\beta_m^{(\ell)}$ for $m \mid \ell$ [42, equation (4.9)]:

$$\beta_m^{(\ell)} = \sum_{d>0: d \mid \ell} \frac{\mu \left(\frac{m}{m \wedge d} \right) \phi \left(\frac{\ell}{d} \right)}{\ell \phi \left(\frac{m}{m \wedge d} \right)} \tilde{\beta}^{(\ell)}, \quad (\text{A.3})$$

where $\tilde{\beta}^{(\ell)} = \beta^{(\ell)}$ for $\ell \geq 2$ [cf. (A.1)], and $\tilde{\beta}^{(1)} = -1$, $m \wedge d$ denotes the greatest common divisor of m, d , and μ and ϕ are the Möbius and Euler's totient functions, respectively. The amplitudes for $0 \leq \ell \leq 5$ are listed (with a slightly different notation) in [53, equations (2.32)/(2.33)]. We will also need the amplitudes for $\ell = 6$, which read:

$$\beta_1^{(6)} = \frac{1}{6} Q(Q-1)(Q-3)(Q^3 - 8Q^2 + 19Q - 11), \quad (\text{A.4a})$$

$$\beta_2^{(6)} = \frac{1}{6} (Q-1)^2(Q-2)(Q^3 - 8Q^2 + 17Q - 3), \quad (\text{A.4b})$$

$$\beta_3^{(6)} = \frac{1}{6} Q(Q-2)(Q-3)(Q-4)(Q^2 - 3Q + 1), \quad (\text{A.4c})$$

$$\beta_6^{(6)} = \frac{1}{6} Q(Q-1)(Q-2)(Q-4)(Q^2 - 5Q + 5), \quad (\text{A.4d})$$

and satisfy $\beta^{(6)} = \beta_1^{(6)} + \beta_2^{(6)} + 2\beta_3^{(6)} + 2\beta_6^{(6)}$.

The amplitudes for $\ell = 0$ are always $\beta^{(0)}$ for $2 \leq L \leq 6$; and the other amplitudes are shown in table A1. For those eigenvalues belonging to a single sector, we always find one of the basic amplitudes (i.e., $\beta^{(0)}$, $\beta^{(1)}$, and $\beta_m^{(\ell)}$; cf. (A.1)/(A.3)/(A.4)), sometimes multiplied by a positive integer multiplicity factor. For those eigenvalues belonging to two sectors, we always find that the corresponding amplitude is a linear combination (with positive integer coefficients) of the basic amplitudes corresponding to those sectors.

L	$\ell = 1$	$\ell = 2$	$\ell = 3$	$\ell = 4$
2	$\beta^{(1)}$	$\beta_1^{(2)}$		
3	$\beta^{(1)}$	$\beta_1^{(2)}, \beta_2^{(2)}$	$\beta_1^{(3)}$	
4	$\beta^{(1)}$	$\beta_1^{(2)}, \beta_2^{(2)}$	$\beta_1^{(3)}, \beta_3^{(3)}, 2\beta_3^{(3)}$	$\beta_1^{(4)}$
5	$\beta^{(1)}$	$\beta_1^{(2)}, \beta_2^{(2)}$	$\beta_1^{(3)}, \beta_3^{(3)}, 2\beta_3^{(3)}$	$\beta_1^{(4)}, \beta_4^{(4)}, 2\beta_4^{(4)}, \beta_2^{(4)}$
6	$\beta^{(1)}, 2\beta^{(1)}$	$\beta_1^{(2)}, 2\beta_1^{(2)}, \beta_2^{(2)}, 2\beta_2^{(2)}$	$\beta_1^{(3)}, 2\beta_1^{(3)}, \beta_3^{(3)}, 2\beta_3^{(3)}$	$\beta_1^{(4)}, \beta_4^{(4)}, 2\beta_4^{(4)}, \beta_2^{(4)}, 3\beta_2^{(4)}$
L	$\ell = 5$	$\ell = 6$	$\ell = L, L - 1$	$\ell = 1, 2$
4			$\beta_1^{(3)} + \beta_4^{(4)}$	
5	$\beta_1^{(5)}$		$\beta_1^{(4)} + \beta_5^{(5)}$	$2(\beta^{(1)} + \beta^{(2)})$
6	$\beta_1^{(5)}, \beta_5^{(5)}, 2\beta_5^{(5)}$	$\beta_1^{(6)}$	$\beta_1^{(5)} + \beta_6^{(6)}$	

Table A1. Amplitudes of the eigenvalues contributing to the chromatic polynomial according to the sector the eigenvalue belongs to. All the eigenvalues belonging to sector $\ell = 0$ have amplitude $\beta^{(0)}$. The results for $2 \leq L \leq 4$ were obtained by Chang and Shrock [87–89], while those for $L = 5, 6$ and the classification in terms of sectors were obtained in [53].

L	$\ell = 1$	$\ell = 2$	$\ell = 3$	$\ell = 4$
2	$\beta^{(1)}$	$\beta_1^{(2)}$		
3	$\beta^{(1)}$	$\beta_1^{(2)}, \beta_2^{(2)}$	$\beta_1^{(3)}, \beta_3^{(3)}$	
4	$\beta^{(1)}$	$\beta_1^{(2)}, \beta_2^{(2)}$	$\beta_1^{(3)}, \beta_3^{(3)}, 2\beta_3^{(3)}$	$\beta_1^{(4)}, \beta_4^{(4)}$

Table A2. Amplitudes of the eigenvalues contributing to the partition function for a triangular-lattice strip on a torus of width $2 \leq L \leq 4$. They are classified according to the sector the eigenvalue belongs to. All the eigenvalues belonging to sector $\ell = 0$ have amplitude $\beta^{(0)}$.

Appendix A.2. Partition function

For the full partition function, we could determine the amplitudes only for $2 \leq L \leq 4$. The results are displayed in table A2. By comparing tables A1 and A2, we find two differences: 1) for $\ell = L \geq 3$ there are more amplitudes in the partition-function case; a fact that is quite natural; and 2) each eigenvalue for $L = 4$ in the partition-function case belongs to a single sector (in particular, when we take $v = -1$, each eigenvalue corresponding to the amplitude $\beta_2^{(4)}$ becomes identical to one of the eigenvalues with amplitude $\beta_1^{(3)}$).

Acknowledgments

We acknowledge useful discussions and correspondence with Yacine Ikhlef, Alan Sokal, Eric Vernier, and Paul Zinn-Justin. We also thank Alan Sokal for the kind permission to use computational resources (provided by Dell Corporation) at New York University.

J.S. is grateful for the hospitality from 2009 to 2017 of the Laboratoire de Physique Théorique at the École Normale Supérieure where part of this work was done.

The research of J.L.J. was supported in part by the Agence Nationale de la Recherche (grant ANR-10-BLAN-0414: DIME), the Institut Universitaire de France, and the European Research Council (through the advanced grant NuQFT). The research of J.L.J. and J.S. was supported in part by Spanish MINECO grant FIS2014-57387-C3-3-P. The work of C.R.S was performed under the auspices of the U.S. Department of Energy at the Lawrence Livermore National Laboratory under Contract No DE-AC52-07NA27344.

References

- [1] Pelissetto A and Vicari E 2002 *Phys. Rep.* **368** 549
- [2] Baxter R J 1982 *Exactly solved models in statistical mechanics* (Academic Press, London)
- [3] Kasteleyn P W 1961 *Physica* **27** 1209
- [4] Stephenson J 1964 *J. Math. Phys.* **5** 1009
- [5] Blöte H W J and Hilhorst H J 1982 *J. Phys. A: Math. Gen.* **15** L631
- [6] Nienhuis B, Hilhorst H J and Blöte H W J 1984 *J. Phys. A: Math. Gen.* **17** 3559
- [7] Assis M, Jacobsen J L, Jensen I, Maillard J M and McCoy B M 2014 *J. Phys. A: Math. Theor.* **47** 445001
- [8] Kondev J, de Gier J and Nienhuis B 1996 *J. Phys. A: Math. Gen.* **29** 6489
- [9] Jacobsen J L and Kondev J 1998 *Nucl. Phys. B* **532** 635
- [10] Kondev J and Jacobsen J L 1998 *Phys. Rev. Lett.* **81** 2922
- [11] Kondev J 1997 *Int. J. Mod. Phys. B* **11** 153
- [12] Potts R B 1952 *Proc. Camb. Phil. Soc.* **48** 106
- [13] Wu F Y 1982 *Rev. Mod. Phys.* **54** 235
- [14] Baxter R J 1973 *J. Phys. C* **6** L445
- [15] Baxter R J, Temperley H N V and Ashley S E 1978 *Proc. R. Soc. London A* **358** 535
- [16] Baxter R J 1982 *Proc. Roy. Soc. London A* **383** 43
- [17] Baxter R J 1986 *J. Phys. A: Math. Gen.* **19** 2821
- [18] Baxter R J 1987 *J. Phys. A: Math. Gen.* **20** 5241
- [19] Jacobsen J L and Saleur H 2006 *Nucl. Phys. B* **743** 207
- [20] Vernier E, Jacobsen J L and Salas J 2016 *J. Phys. A: Math. Theor.* **49** 174004
- [21] Saleur H 1991 *Nucl. Phys. B* **360** 219
- [22] Francesco P D, Mathieu P and Sénéchal D 1997 *Conformal Field Theory* (Springer-Verlag, New York)
- [23] Pasquier V 1987 *J. Phys. A* **20** L1229
- [24] Saleur H and Bauer M 1989 *Nucl. Phys. B* **320** 591
- [25] Pasquier V and Saleur H 1990 *Nucl. Phys. B* **330** 523
- [26] Fortuin C M and Kasteleyn P W 1972 *Physica* **57** 536
- [27] Chang S C, Salas J and Shrock R 2002 *J. Stat. Phys.* **107** 1207
- [28] Chang S C, Jacobsen J L, Salas J and Shrock R 2004 *J. Stat. Phys.* **114** 763
- [29] Jacobsen J L and Salas J 2013 *J. Combin. Theory B* **103** 532
- [30] Jacobsen J L and Scullard C R 2012 *J. Phys. A: Math. Theor.* **45** 494003
- [31] Jacobsen J L and Scullard C R 2013 *J. Phys. A: Math. Theor.* **46** 075001
- [32] Jacobsen J L 2014 *J. Phys. A: Math. Theor.* **47** 135001
- [33] Jacobsen J L 2015 *J. Phys. A: Math. Theor.* **48** 454003
- [34] Scullard C R and Jacobsen J L 2016 *J. Phys. A: Math. Theor.* **49** 125003
- [35] Tutte W T 1954 *Can. J. Math.* **6** 81
- [36] Jacobsen J L, Salas J and Sokal A 2005 *J. Stat. Phys.* **119** 1153
- [37] Jacobsen J L 2010 *J. Phys. A: Math. Theor.* **43** 315002
- [38] Vernier E and Jacobsen J L 2012 *J. Phys. A: Math. Theor.* **45** 045003

- [39] Jacobsen J L 2009 Conformal field theory applied to loop models, *in* Polygons, polyominoes and polycubes, *Lecture Notes in Physics* vol **775** ed Guttmann A J (Heidelberg: Springer Verlag) pp 347–424
- [40] Nienhuis B 1984 *J. Stat. Phys.* **34** 731
- [41] Richard J F and Jacobsen J L 2006 *Nucl. Phys. B* **750** 250
- [42] Richard J F and Jacobsen J L 2007 *Nucl. Phys. B* **769** 256
- [43] Pasquier V 1988 *Commun. Math. Phys.* **118** 355
- [44] Ikhlef Y, Jacobsen J L and Saleur H 2008 *Nucl. Phys. B* **789** 483
- [45] Ikhlef Y, Jacobsen J L and Saleur H 2012 *Phys. Rev. Lett.* **108** 081601
- [46] Witten E 1991 *Phys. Rev. D* **44** 314
- [47] Dijkgraaf R, Verlinde H and Verlinde E 1992 *Nucl. Phys. B* **371** 269
- [48] Vernier E, Jacobsen J L and Saleur H 2014 *J. Phys. A: Math. Theor.* **47** 285202
- [49] Vernier E, Jacobsen J L and Saleur H 2015 *J. Stat. Mech.: Theor. Exp.* **2015** P09001
- [50] Salas J and Sokal A D 2001 *J. Stat. Phys.* **104** 609
- [51] Jacobsen J L and Salas J 2001 *J. Stat. Phys.* **104** 701
- [52] Jacobsen J L and Salas J 2006 *J. Stat. Phys.* **122** 705
- [53] Jacobsen J L and Salas J 2007 *Nucl. Phys. B* **783** 238
- [54] Salas J and Sokal A D 2009 *J. Stat. Phys.* **135** 279
- [55] Beraha S, Kahane J and Weiss N J 1975 *Proc. Nat. Acad. Sci. USA* **72** 4209
- [56] Beraha S, Kahane J and Weiss N J 1978 Limits of zeroes of recursively defined families of polynomials, *in* Studies in Foundations and Combinatorics, *Advances in Mathematics Supplementary Studies* vol **1** ed Rota G C (New York: Academic Press) pp 213–232
- [57] Beraha S, Kahane J and Weiss N J 1980 *J. Combin. Theory B* **28** 52
- [58] Jacobsen J L and Saleur H 2008 *J. Stat. Phys.* **132** 707
- [59] Duplantier B and David F 1988 *J. Stat. Phys.* **51** 327
- [60] Caracciolo S, Jacobsen J L, Saleur H, Sokal A D and Sportiello A 2004 *Phys. Rev. Lett.* **93** 080601
- [61] Jacobsen J L and Saleur H 2005 *Nucl. Phys. B* **716** 439
- [62] Saleur H 1990 *Commun. Math. Phys.* **132** 657
- [63] Jacobsen J L, Salas J and Sokal A D 2003 *J. Stat. Phys.* **112** 921
- [64] Nienhuis B 1982 *Phys. Rev. Lett.* **49** 1062
- [65] Fateev V A and Zamolodchikov A B 1987 *Nucl. Phys. B* **280** 644
- [66] Zamolodchikov A B and Fateev V A 1987 *Theor. Math. Phys.* **71** 451
- [67] Jacobsen J L and Salas J 2013 *Nucl. Phys. B* **875** 678
- [68] Halverson T and Ram A 2005 *Eur. J. Comb.* **26** 869
- [69] Scullard C R and Jacobsen J L 2012 *J. Phys. A: Math. Theor.* **45** 494004
- [70] Scullard C R and Ziff R M 2008 *Phys. Rev. Lett* **100** 185701
- [71] Scullard C R 2012 *J. Stat. Mech.: Theor. Exp.* **2011** P09022
- [72] Scullard C R 2012 *Phys. Rev. E* **86** 041131
- [73] Scullard C R 2012 *J. Stat. Mech.: Theor. Exp.* **2012** P11011
- [74] Salas J and Sokal A D 2011 *J. Stat. Phys.* **144** 1028
- [75] Sokal A D 2004 *Combin. Prob. Comput.* **13** 221
- [76] Lehoucq R B, Sorensen D C and Yang C 1998 *ARPACK users' guide: solution of large-scale eigenvalue problems with implicitly restarted Arnoldi methods* (Society for Industrial and Applied Mathematics)
- [77] Haible B and Kreckel R 1996 URL: <http://www.ginac.de/CLN>
- [78] Kostov I K 1989 *Nucl. Phys. B* **326** 583
- [79] Jacobsen J L, Richard J F and Salas J 2006 *Nucl. Phys. B* **743** 153
- [80] Jacobsen J L and Sokal A D 2008 *unpublished*
- [81] Pasquier V 1987 *Nucl. Phys. B* **285** 162
- [82] Richard J F and Jacobsen J L 2005 *Nucl. Phys. B* **731** 335
- [83] Temperley H N V and Lieb E H 1971 *Proc. R. Soc. London A* **322** 251

- [84] Belletête J, Gainutdinov A G, Jacobsen J L, Saleur H and Vasseur R 2017 *in preparation*
- [85] Adler J, Brandt A, Janke W and Shmulyian S 1995 *J. Phys. A: Math. Gen.* **28** 5117
- [86] Dubail J, Jacobsen J L and Saleur H 2010 *J. Phys. A: Math. Theor.* **43** 482002
- [87] Chang S C and Shrock R 2006 *Physica* **369** 231
- [88] Chang S C and Shrock R 2006 *Physica* **292** 307
- [89] Chang S C and Shrock R 2001 *Ann. Phys. (N.Y.)* **290** 124